



**HAL**  
open science

## New approach for coupling $k-2$ and empirical Green's functions: application to the blind prediction of broad-band ground motion in the Grenoble basin

Mathieu Causse, Emmanuel Chaljub, Fabrice Cotton, Cécile Cornou,  
Pierre-Yves Bard

### ► To cite this version:

Mathieu Causse, Emmanuel Chaljub, Fabrice Cotton, Cécile Cornou, Pierre-Yves Bard. New approach for coupling  $k-2$  and empirical Green's functions: application to the blind prediction of broad-band ground motion in the Grenoble basin. *Geophysical Journal International*, 2009, 179 (3), pp.1627 - 1644. 10.1111/j.1365-246X.2009.04354 . insu-00498638

**HAL Id: insu-00498638**

**<https://insu.hal.science/insu-00498638>**

Submitted on 5 Mar 2021

**HAL** is a multi-disciplinary open access archive for the deposit and dissemination of scientific research documents, whether they are published or not. The documents may come from teaching and research institutions in France or abroad, or from public or private research centers.

L'archive ouverte pluridisciplinaire **HAL**, est destinée au dépôt et à la diffusion de documents scientifiques de niveau recherche, publiés ou non, émanant des établissements d'enseignement et de recherche français ou étrangers, des laboratoires publics ou privés.

# New approach for coupling $k^{-2}$ and empirical Green's functions: application to the blind prediction of broad-band ground motion in the Grenoble basin

Mathieu Causse, Emmanuel Chaljub, Fabrice Cotton, Cécile Cornou and Pierre-Yves Bard

Laboratoire de Géophysique Interne et de Tectonophysique (LGIT), CNRS, Université Joseph Fourier, Observatoire des Sciences de l'Univers de Grenoble, Institut de recherche pour le Développement, Laboratoire Central des Ponts-et-Chaussées, France. E-mail: mathieu.causse@obs.ujf-grenoble.fr

Accepted 2009 August 3. Received 2009 May 13; in original form 2008 June 2

## SUMMARY

We present a new approach for performing broad-band ground motion time histories (0.1–30 Hz) of a future earthquake in a sedimentary basin. Synthetics are computed with an hybrid scheme combining reciprocity-based 3-D-spectral element method simulations at low frequencies and empirical Green's functions (EGF) at high frequencies. The combination between both deterministic and empirical parts results in a set of hybrid Green's functions, summed according to a new  $k^{-2}$  kinematic model algorithm. The summation technique enables to remove the high-frequency artefacts that appear above the EGF corner frequency. The ground motion variability is assessed by generating a variety of source parameter sets selected from *a priori* probability density functions. This leads to a population of response spectra, from which the median spectral acceleration and standard deviation values are derived. The method is applied to simulate a  $M_W$  5.5 event in the deep Grenoble basin (French Alps). The comparison with EC8 regulations suggests the need of specific design spectra in the Grenoble valley.

**Key words:** Earthquake ground motions; Site effects; Europe.

## INTRODUCTION

Synthesizing time histories of ground motion in urban areas is useful to design specific structures and to estimate potential damages for a future earthquake. This is particularly true in European alpine valleys where moderate earthquakes may have large consequences caused by large 2-D/3-D site effects. The Grenoble city is a typical example of alpine valley: first, historic seismicity shows the possibility of  $M_W$  5.5 events at the vicinity of the city ( $\approx 20$  km); second, this deep sedimentary valley exhibits large complex site effects (Lebrun *et al.* 2001; Cornou *et al.* 2003; Guéguen *et al.* 2006b; Drouet *et al.* 2007). In order to analyse seismic hazard in the Grenoble valley, a  $M_W$  5.5 scenario earthquake occurring on the Belledonne border fault south of the city is assumed (Thouvenot *et al.* 2003). The source proximity makes it necessary to use a finite-extent source description. The ground motion predictions are thus performed with a new approach coupling the  $k^{-2}$  source model (Herrero & Bernard 1994) and hybrid Green's functions (HGF), that incorporate 3-D site effects. This new procedure provides an estimation of the ground motion variability.

Ground motion characteristics are strongly affected by the velocity structure. The lack of detailed knowledge of the propaga-

tion medium makes it usually difficult to use numerical methods for estimating ground motion at high frequency (generally above 1–2 Hz). An alternative approach is then the empirical Green's functions (EGF) method (Hartzell 1978), when good quality small earthquake recordings are available. This method automatically includes propagation and site effects, under the assumption of the soil response linearity. Nevertheless it is inadequate for assessing low-frequency ground motion, because of the often bad signal-to-noise ratio in the small event recordings below 1 Hz. Thus, several authors (Kamae *et al.* 1998; Pulido & Kubo 2004; Pacor *et al.* 2005) proposed to calculate broad-band ground motion with a hybrid scheme combining deterministic and stochastic approaches: low-frequency Green's functions are evaluated by numerical algorithms whereas high-frequency Green's functions are obtained from filtered white noise. In this paper, a hybrid method is also proposed. First, low-frequency ground motion ( $< 1$  Hz) is modelled with 3-D spectral element method (Komatitsch & Vilotte 1998; Komatitsch & Tromp 1999; Komatitsch *et al.* 2004; Chaljub *et al.* 2007) calculations based on reciprocity. Second, the good quality recordings of a  $M_L$  2.8 earthquake provided by the 2005 Grenoble experiment (Chaljub *et al.* 2006) and the French permanent accelerometric network (<http://www-rap.obs.ujf-grenoble.fr>),

are used as EGFs to simulate high-frequency ground motion (1–30 Hz). The advantage of such a combination is that both methods are adequate for simulating specific site effects.

In addition, in the relevant frequency range for earthquake engineering and within a few fault lengths, ground-motion simulations highly depend on the rupture process complexity. Thanks to its ease of application, kinematic modelling remains the best way to perform physically based ground motion predictions. Moreover, Hartzell *et al.* (2005) compared a class of kinematic models based on fractal distribution of subevent sizes with a simple slip-weakening dynamic model and concluded that at present the kinematic simulations match better the 1994 Northridge ground motion than the dynamic ones. A now classical approach is a self-similar rupture model in which the spatial static slip distribution is described in the wavenumber domain by a  $k^{-2}$  power-law decay (Herrero & Bernard 1994; Bernard *et al.* 1996). This model leads to the commonly observed  $\omega^{-2}$  displacement amplitude spectrum decay under the two constraints that the rupture front propagates with a constant rupture velocity and that the rise time is inversely proportional to the wavenumber  $k$ . Ground motion is next computed by summing up the HGF according to a  $k^{-2}$  source model. In order to couple  $k^{-2}$  model and the EGF method, a specific summation algorithm is developed. It enables to correct the high-frequency artefacts that appear above the EGF corner frequency. Finally, source parameters are defined with probability density functions and the resulting ground motion variability is assessed by means of the Latin Hypercube Sampling (LHS) method. The ground motion sensitivity to source parameters and to EGF uncertainties is thoroughly investigated. As a result, median and standard deviation of the spectral acceleration (SA) are predicted on nine stations within the Grenoble valley in the frequency range [0.1–30 Hz]. In order to test the reliability of the ground motion predictions, simulations on rock station are compared to the empirical ground motion equations developed by Bragato & Slejko (2005) and to the stochastic method of Pousse *et al.* (2006). The comparison of the predictions at sediments stations with Eurocode eight suggests the need of specific design spectra in the framework of the Grenoble basin.

## SOURCE MODEL

### Static slip distribution

The complexity of the static slip is described with a self-similar distribution of slip heterogeneities. Following Herrero & Bernard (1994) the static slip is supposed to have a  $k^{-2}$  asymptotic decay in the wavenumber domain beyond the corner wavenumber  $k_c$ , inversely proportional to the ruptured fault dimension. For a rectangular fault plane with length  $L$  and width  $W$  we define the slip amplitude spectrum in a way similar to Somerville *et al.* (1999) and Galovic & Brokesova (2004)

$$D_k(k_x, k_y) = \frac{\bar{D}LW}{\sqrt{1 + \left[ \left( \frac{k_x L}{K} \right)^2 + \left( \frac{k_y W}{K} \right)^2 \right]^2}}, \quad (1)$$

where  $k_x$  and  $k_y$  are the wavenumbers along the strike and the dip directions, respectively,  $\bar{D}$  refers to the mean slip and  $K$  is a dimensionless constant controlling the corner wavenumber  $k_c = K/\sqrt{(L^2 + W^2)}$ . The parameter  $K$  is fundamental because it determines the amplitude of the slip heterogeneities generating the high-frequency source energy. At low wavenumber [ $k_x^2 + k_y^2 \leq$

$(1/L)^2 + (1/W)^2$ ] the slip spectrum phases are chosen to concentrate the slip on the fault centre whereas for high wavenumbers, phases are random. Consequently, the static slip is the sum of a deterministic and a stochastic part. The deterministic part of the slip generates a smooth asperity with mean slip  $\bar{D}$ , the size of which depends on the corner wavenumber, that is, the dimensionless parameter  $K$ . Large values of  $K$  lead to a small asperity. The main asperity is then added to the high wavenumber slip contributions, corresponding to a set of zero mean slip heterogeneities. This leads to a variety of heterogeneous slip models. All the details to generate the static slip distributions can be found in Appendix A.

Since for a given wavenumber  $k > k_c$ , the slip fluctuation amplitudes are proportional to  $K^2$ ,  $K$  controls the roughness of the static slip. Fig. 1 displays examples of static slip distributions obtained for different  $K$  values. The case  $K = 0.35$  results in one large smooth asperity covering the whole fault plane. For  $K = 1.4$  the maximum slip increases and a large part of the fault has zero slip. Consequently, the gradient of the slip distribution increases as well and static slip is rougher. This emphasizes the link between  $K$  and the average static stress drop  $\Delta\sigma$ . To better illustrate this correlation,

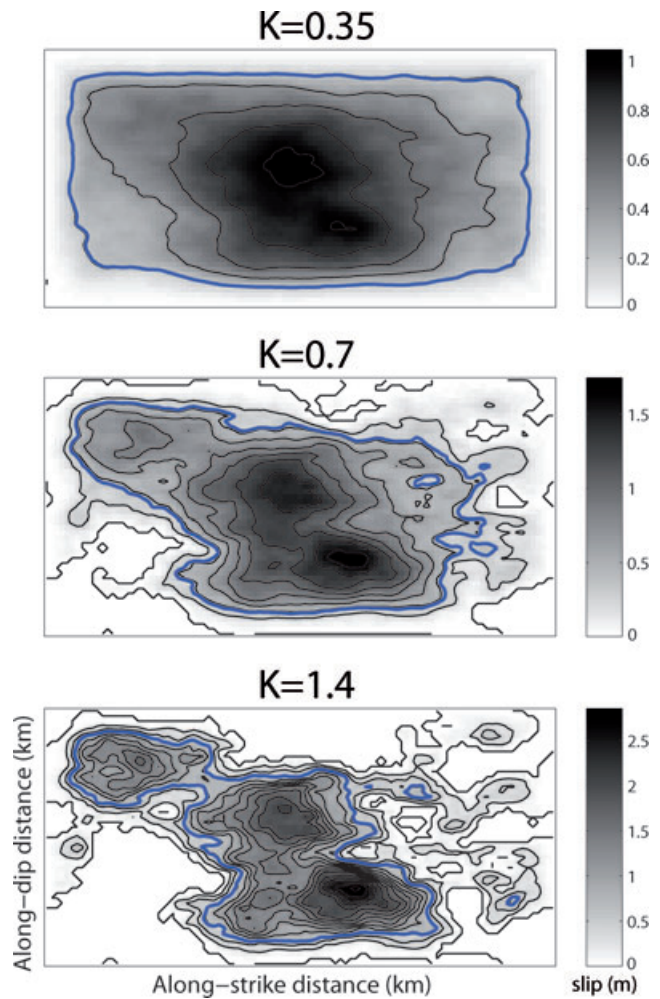


**Figure 1.** Example of static slip distributions for different  $K$  values. The mean slip is  $\bar{D} = 0.4$  m in all cases. The blue line defines the area with slip above  $0.2D_{\max}$ . To calculate the static stress drop values, we assume  $C_f = 1$  and  $\mu = 10^{10}$  N m. The  $\Delta\sigma$  values are 18, 34 and 65 bars for  $K = 0.35$ , 0.7 and 1.4, respectively.

we calculate  $\Delta\sigma$  following Kanamori & Anderson (1975):

$$\Delta\sigma = C_f \mu \frac{\bar{D}}{\bar{L}}, \quad (2)$$

where  $C_f$  is a non-dimensional shape factor ( $C_f \approx 1$  in all cases),  $\mu$  is the rigidity and  $\bar{L}$  represents the characteristic length of the rupture area. We define  $\bar{L}$  as the square root of the main slip area, defined by the fault surface with slip over 20 per cent of the maximum slip. This simple test shows the average static stress drop increase with  $K$  (see legend of Fig. 1 for more details).

### Source kinematics

Following Bernard *et al.* (1996), we model the rupture process as a ‘self-healing’ slip pulse of width  $L_0$  propagating at constant rupture velocity  $v$ . For wavenumbers  $k < \frac{1}{2L_0}$ , the rise time is  $\tau_{\max} = L_0/v$  whereas for higher wavenumbers, the rise time is inversely proportional to  $k$ . These choices ensure the commonly observed flat level of the acceleration amplitude spectrum beyond the corner frequency  $F_c$ . Gallovic & Brokesova (2004) derived a general equation of the ground motion acceleration spectrum for a 2-D rectangular fault model with a  $k$ -dependent rise time. They developed an analytical formula of the amplitude spectrum for a line fault in a homogeneous elastic medium, in the Fraunhofer’s approximation. The authors show evidence of two characteristic frequencies. First, the corner frequency can be expressed as

$$F_c = \frac{vC_dK}{L}, \quad (3)$$

where  $C_d = \frac{1}{1-(v/c)\cos\Theta}$  is the directivity coefficient (Ben-Menahem 1961).  $\Theta$  denotes the directivity angle, defined as the angle between the rupture front propagation and the source–receiver direction, and  $c$  is the shear wave velocity. The second characteristic frequency is defined as:  $F_l = (vC_d)/(2L_0)$ . Beyond  $F_l$ , the high-frequency energy comes from the coherent summation of the small-scale ruptures within the slip band. Gallovic & Burjanek (2007) showed that such constructive interferences result in overestimated high-frequency directivity effects. Thus, following Bernard & Herrero (1994) and Gallovic & Burjanek (2007), we assign the small-scale heterogeneities ( $k > \frac{1}{2L_0}$ ) random rupture directions to reduce the high-frequency spectral level dependence on the rupture propagation direction. According to Gallovic & Burjanek (2007), at frequencies above the transition frequency

$$F_0 = \frac{v}{L_0} = \frac{1}{\tau_{\max}}, \quad (4)$$

the acceleration amplitude spectral level for  $\Theta = 0^\circ$  and  $\Theta = 180^\circ$  is such that

$$A_0 = 4\pi^2 C_s M_0 \left(\frac{v}{L}\right)^2 \cdot K^2 \cdot \text{RMS} [C_d(\Theta)^2 X(C_d(\Theta)/2)], \quad (5)$$

where  $C_s$  contains the propagation information and radiation pattern and  $X$  is the amplitude spectrum of the slip velocity function corresponding to unit slip and a one second rise time. In this paper, a Gaussian function with standard deviation  $\sigma = \tau_{\max}/10$  is assumed for the slip velocity function. For  $\Theta = 90^\circ$ , the spectral level is flat above the corner frequency. It is given by

$$A_{\Theta=90^\circ} = 4\pi^2 C_s M_0 \left(\frac{v}{L}\right)^2 \cdot K^2 \cdot X(1/2). \quad (6)$$

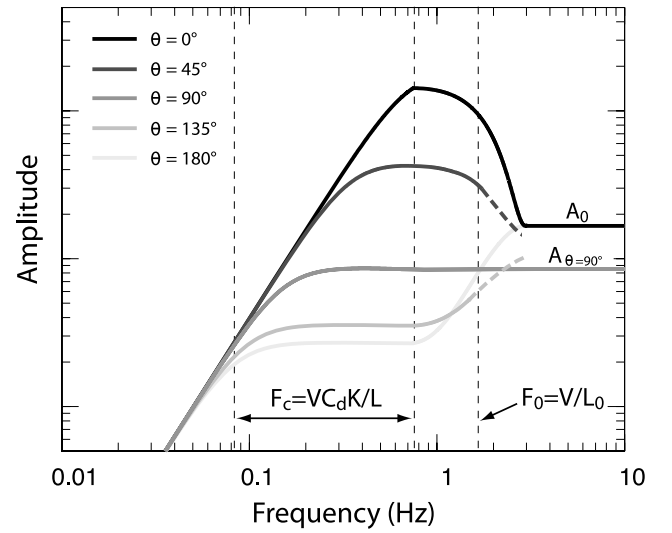


**Figure 2.** Representation of the acceleration spectra for different values of the directivity angle  $\Theta$ . A Gaussian slip velocity function with standard deviation  $\sigma = \tau_{\max}/10$  is assumed. In this example,  $L = 20$  km,  $K = 1$ ,  $L_0 = 0.1L$ ,  $v = 3000$  m s $^{-1}$  and  $v/c = 0.8$ . Introducing rupture incoherence does not modify the spectrum for  $\Theta = 90^\circ$ . Nevertheless, for  $\Theta = 0^\circ$  and  $180^\circ$ , the directivity coefficient is the quadratic sum of  $C_d^2$  coefficients with variable  $\Theta$  (Bernard & Herrero 1994). To obtain the curves for  $\Theta = 0^\circ$  and  $180^\circ$ , following Gallovic & Burjanek (2007), the theoretical spectra for a classical  $k^{-2}$  model are modified by setting their level to  $A_0$  above the frequency  $2f_0$ . A cosine function is then applied between frequencies  $f_0/2$  and  $2f_0$  to ensure a smooth transition. The high-frequency levels for the other values of  $\Theta$  range from  $A_{\Theta=90^\circ}$  to  $A_0$ .

The levels obtained for the other values of  $\Theta$  range from  $A_0$  to  $A_{\Theta=90^\circ}$ . A representation of the ground acceleration amplitude spectrum is given in Fig. 2. The whole rupture process is illustrated on Fig. 3. Note that the resulting slip velocity functions exhibits negative values at some points, which is physically unrealistic. Ruiz *et al.* (2007) developed a recombination scheme of the Fourier slip components to get slip velocity functions compatible with earthquake dynamic (e.g. Tinti *et al.* 2005). Nevertheless, studying the shape of this function is not the purpose of our study and we do not apply any other correction than removing the negative slip values.

### SUMMATION ALGORITHM

The simulated event ground motion displacement  $U(r, t)$  at position  $r$  is numerically expressed according to the discretized representation theorem (Aki and Richards 2002)

$$U(r, t) = \sum_{ij} \frac{\mu_{ij} a_{ij}}{m_{oij}} s_{ij}(t - t_{rij}) * G_{ij}(r, t), \quad (7)$$

where  $\mu_{ij}$ ,  $a_{ij}$ ,  $m_{oij}$  and  $G(r, t)_{ij}$  refer to the rigidity, area, seismic moment and Green’s function at the subfault  $(i, j)$ , respectively. The slip histories  $s_{ij}(t)$  and the rupture times  $t_{rij}$  arise from the  $k^{-2}$  source model described above. In this study  $G_{ij}(r, t)$  is replaced with the recording of a small earthquake  $u(r, t)$  used as EGF. According to Hartzell (1978) the summation is valid only below the EGF corner frequency  $f_c$ . The small event is supposed to follow a  $k^{-2}$  model as well. In the following  $(l, w, K_S, \bar{d}, m_o)$  stands for the fault length, width,  $K$  value, mean dislocation and seismic moment of the small event, respectively.

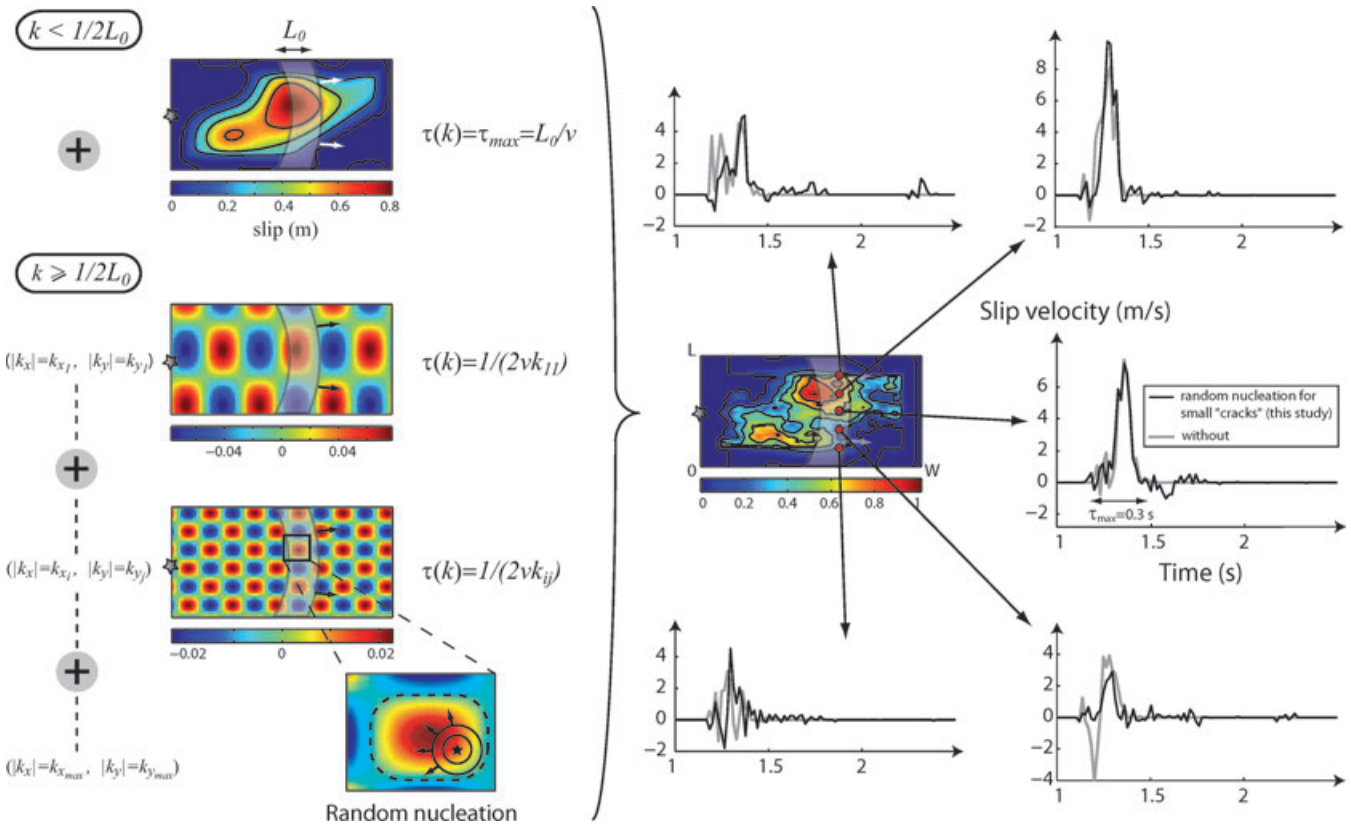


**Figure 3.** Representation of the rupture process, modelled as a slip pulse propagating at constant rupture velocity  $v$ . The slip distribution is split into its low and high components at frequency  $k = \frac{1}{2L_0}$ . The low wavenumber slip has a rise time equal to  $\tau_{\max} = L_0/v$ . The high wavenumber slip is composed of a set of heterogeneities of different scales, considered as independent subevents. These subevents start slipping as the main rupture front reaches one point, randomly chosen, from which a secondary rupture front propagates (see bottom left box). The slip duration for a given subevent is proportional to its wavenumber. The figure also displays example of resulting slip velocity functions, compared with the functions that would be obtained from a classical  $k^{-2}$  model (without random nucleation points). In this example,  $L = 5$  km,  $W = 2.5$  km,  $\bar{D} = 0.2$  m,  $K = 1$  and  $\tau_{\max} = 0.3$  s.

### Fault plane discretization

The EGF fault plane is assumed to be a square. Its length is determined from the corner frequency. The EGF is supposed to be small enough ( $M_L = 2.8$  in this study) to neglect directivity effects. This common assumption is controversial (e.g. Boatwright 2007) and is discussed in the section ‘EGF uncertainties’. Thus, assuming a  $k^{-2}$  model, the EGF corner frequency is such that

$$f_c = \frac{vK_S}{l}. \quad (8)$$

Assessing the rupture length implies to determine the  $K_S$  value. An approximation of  $K_S$  can be obtained by considering the model of Brune (1970), which gives for a circular fault:  $f_c = 0.33c/r_{fge}$ , where  $c$  is the shear wave velocity and  $r_{fge}$  is the fault radius. In the case of a square fault plane, the conservation of the EGF rupture surface between a square and a circular fault gives:  $f_c = 0.33\sqrt{\pi}c/l$ . By considering:  $v = 0.8c$ , which is consistent with dynamic rupture modelling, we get:  $f_c \approx 0.74v/l$ . This suggests  $K_S \approx 0.74$ . Thus, from eq. (8), we obtain the small earthquake rupture length.

The dimensions of the target event fault plane are next assessed using the scaling laws between small and large earthquakes. The classical law of Brune (1970), based on the assumption of self-

similarity between the small and the large events, gives

$$\frac{L}{l} = \frac{W}{w} = \frac{\bar{D}}{d} = N, \text{ with } N = \left(\frac{M_0}{m_0}\right)^{1/3}. \quad (9)$$

$M_0$  denotes the seismic moment of the target event. Note that eq. (9) is valid provided that both events have the same  $K$  value. In other words, the choices  $L = W = N \cdot l$  and  $K = K_S$  lead to a target event stress drop equal the EGF one. In our procedure,  $L$  and  $W$  are fixed. Consequently, the natural variability of the simulated event stress drop is accounted for by a deviation from  $K = K_S$ . The choice of the  $K$  value distribution will be discussed later. The fault plane discretization parameters can be found in Table 1.

### Summation along dislocation rise-time

As explained above, the static slip consists in a deterministic part, with mean slip  $\bar{D}$  and a stochastic zero mean high wavenumber part. It leads us to split the summation along the dislocation rise-time in two parts. The number of EGFs to sum on a given subfault ( $i, j$ ) is:  $N_{ij} = N_{\text{DET},ij} + N_{\text{STO},ij}$ , where DET and STO indices stand for deterministic and stochastic slip, respectively.  $N_{\text{DET},ij}$  is such that  $\sum_{ij} N_{\text{DET},ij} = N^3$  and  $N_{\text{STO},ij} = \sum_k \frac{1}{2} |D_{kij}|$ , where  $D_{kij}$  is the slip contribution of the  $k$ th spectrum component at the subfault ( $i, j$ ). The global summation algorithm can be expressed as

$$U(r, t) = R(t) * u(r, t), \quad (10)$$

**Table 1.** Fault plane discretization and EGF parameters.  $N_L$ ,  $N_W$  and  $N_D$  denotes the EGF number to sum along the strike, the dip and the dislocation rise time, respectively.

Parameters	Value
$M_0$	$2.2 \times 10^{17}$ N m
$m_0$	$2.0 \times 10^{13}$ N m
$L/W$	2
$f_c$	12 Hz
$l$	0.160 km
$N_L$	36
$N_W$	18
$N_D$	18
Target event strike	120°
EGF strike	160°
Dip	90°
EGF focal depth	3 km

*Notes:* The seismic moments of the EGF and the simulated event are directly obtained from the moment magnitude. We assume that local magnitude and moment magnitude are the same for the EGF. The corner frequency  $f_c$  is assessed from the EGF displacement amplitude spectrum.

where the site-dependent apparent source-time function (ASTF)  $R(t)$  is

$$R(t) = \sum_{i=1}^N \sum_{j=1}^N \frac{r}{r_{ij}} \left[ \sum_{q=1}^{N_{DET_{ij}}} \delta(t - t_{r_{ij}} - t_{s_{ij}} - t_{DET_q}) + \sum_{q=1}^{N_{STO_{ij}}} p \cdot \delta(t - t_{r_{ij}} - t_{s_{ij}} - t_{STO_q}) \right]. \quad (11)$$

The indice  $q$  denotes the summation along the dislocation rise time. The constant  $p$  is defined according to:  $p = 1$  for  $D_{k_{ij}} > 0$  and  $p = -1$  for  $D_{k_{ij}} < 0$ . At last the term  $t_{s_{ij}}$  is introduced to account for the different subfault/receiver  $S$ -wave traveltime delays and  $r/r_{ij}$  is the geometric spreading factor.

### Summation process beyond the EGF corner frequency

Beyond  $f_c$  the main event energy is purely stochastic because the EGF summation becomes incoherent. Hence the ASTF spectral level is flat and corresponds approximately to the square root of the total number of EGFs to sum up. Thus the resulting high-frequency level is not in agreement with the desired level for the source model. The theoretical level expected for  $f \geq f_c$  is  $\Theta$ -dependent (see section ‘Source kinematics’). However, for simplicity, we assume that this level is the same whatever the value of  $\Theta$  is. We then set the acceleration spectrum level to its maximum value  $A_0$  (note that after eqs (5) and (6), the largest error induced corresponds to a factor of  $A_0/A_{\Theta=90^\circ} \approx 2$ ). Consequently, the theoretical ASTF level is supposed to be (see Appendix B)

$$|R(f \geq f_c)_{\text{theo}}| = \beta N K^2, \quad (12)$$

where  $\beta \approx 3.5$ .

Following Kohrs-Sansorny *et al.* (2005), the number of EGFs to sum along the dislocation rise time is modified to reproduce the required high-frequency spectral level. The following procedure is proposed (see Appendix C): (1) the EGF dislocation  $d$  is adapted so that the average number of EGF summed on each subfault is not

$N$  but  $[\frac{\alpha(N)}{\beta}]^2 \cdot \frac{N^2}{K^2}$ , where  $\alpha(N) = 2\sqrt{\ln(\frac{N-1}{4})}$  and  $\beta \approx 3.5$ ; (2) the deterministic slip contribution to the ASTF is low-pass filtered to keep only the zero mean slip fluctuations contributions beyond  $f_c$  and (3) the spectrum is divided by  $[\frac{\beta}{\alpha(N)}]^2 \cdot \frac{K^2}{N}$  to conserve the seismic moment.

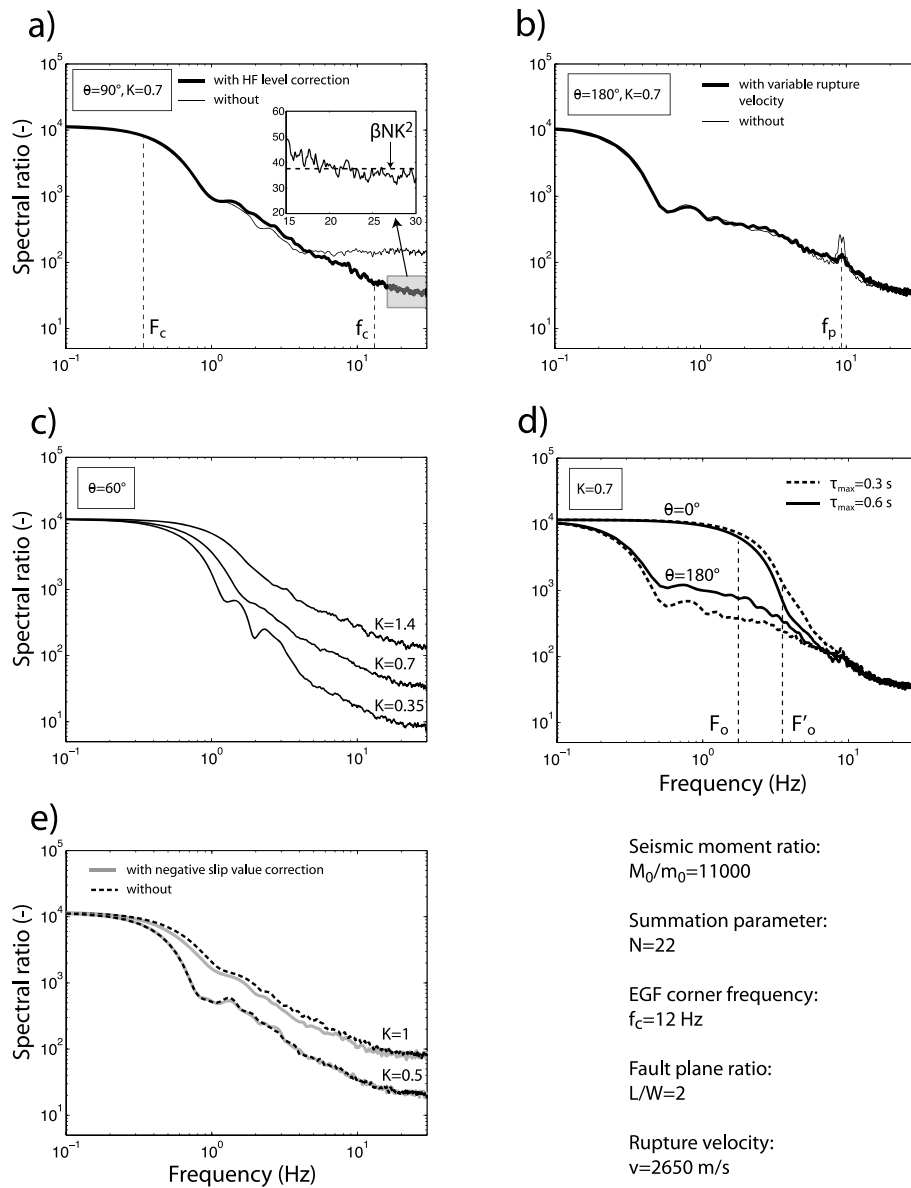
### Resulting ASTF

Fig. 4(a) displays the effects of the above-described EGF summation scheme correction on the average ASTF amplitude spectra. The spectra are calculated for an unilateral rupture and a rectangular fault with  $L/W = 2$ . This fault ratio is in agreement with the results of Somerville *et al.* (1999) and will be kept in the following. Fig. 4(a) shows that the high-frequency procedure based on the assumption of a square fault plane holds for  $L/W = 2$  and the target high-frequency level is reached. Note that in addition to the misestimation of the high-frequency spectral level, another type of numerical artefact appears due to the finite distances between the small-event sources (Bour & Cara 1997). It corresponds to a peak occurring approximately at:  $f_p = vC_d/l$  (Fig. 4b). In order to reduce this peak, a random component is introduced in the rupture velocity  $v$ .  $v$  is thus uniformly distributed in the interval  $[v - 100 \text{ m s}^{-1}, v + 100 \text{ m s}^{-1}]$ . Are also shown the effects of the source (Figs 4c and d). These figures show that the main theoretical characteristics of the amplitude spectrum for a line fault are preserved (i.e. corner frequencies,  $\Theta$ ,  $K$  and  $\tau_{\text{max}}$ -dependence of the model). It should be noticed that  $R(f)$  phases are necessarily stochastic beyond  $f_c$ . Nevertheless this is consistent with the rupture process that is purely stochastic above  $F_0$ .

## GREEN'S FUNCTIONS

### EGFs

On 2005 October 1 a small earthquake occurred on the southern tip of the Belledonne border fault, about 15 km south of the Grenoble city ( $M_L = 2.8$ , Local magnitude Sismalp, <http://sismalp.obs.ujf-grenoble.fr>). This event has been recorded by the French accelerometric permanent network and by a temporary array from the French mobile network (INSU/CNRS), composed of velocimetric sensors (CMG40T, with a flat response from 20 to 60 s) and deployed in the Grenoble city from 2005 June 15 to October 30 (Chaljub *et al.* 2006). These good quality recordings provide an opportunity to simulate the effects of a moderate sized earthquake with the EGF method. Velocities are first differentiated to get the ground acceleration. Twenty-seven three-component accelerograms are then used as EGFs to compute ground motion at nine stations in the Grenoble city (Fig. 5). Seven of the stations are installed on soft soil within the sediment-filled valley, while two are located at rock sites. The hypothesized scenario is a  $M_W$  5.5 left-lateral strike slip event. The fault plane is supposed to be vertical with a strike of 120°. The small earthquake characteristics and the rupture plane discretization parameters are displayed in Table 1. Note that the strike of the small event (160°) is different from that of the target event. Indeed a value of 120° seems more appropriate for a  $M_W$  5.5 scenario in the Laffrey area (Thouvenot *et al.* 2003). In order to account for differences in focal mechanism, a simple procedure is applied to correct the EGF radiation pattern. It has been observed that the radiation pattern of small earthquakes is frequency dependent and characterized by a transition from the theoretical double-couple



**Figure 4.** Average apparent source-time function spectra (quadratic mean of 100 simulated spectra) in the case of an unilateral rupture and a rectangular fault plane with  $L/W = 2$ . The parameters used to compute the spectra are in agreement with the Grenoble application. They are displayed at the bottom right. (a) Effect of the high-frequency spectral level correction. The dashed line in the zoomed box indicates the expected theoretical level. (b) Effect of the addition of a random component to the rupture velocity. (c) Effect of the roughness parameter  $K$ . (d) Effect of the angle  $\Theta$  and the rise time  $\tau_{max}$ . Frequencies  $f_0$  and  $f'_0$  denotes the transition frequencies for  $\tau_{max} = 0.6$  and  $0.3$  s, respectively. (e) Effect of removing the negative slip value.

radiation pattern at low frequencies to a totally isotropic radiation pattern at high frequencies (Sato 2002). Following Pulido & Kubo (2004) we assume a radiation pattern with a linear variation from 1 to 3 Hz between the theoretical double-couple radiation and a spherical radiation. We only consider the contributions of the  $SH$  and  $SV$  waves. The theoretical radiation patterns  $F^{SH}$  and  $F^{SV}$  are given in Aki and Richards (2002) (equations 4.90 and 4.91). To estimate the take-off angle, an homogeneous medium is hypothesized. Finally, to assess the contributions of the  $SH$  and  $SV$  waves to the different ground motion components, we assume a vertically incident wave-field, which is the most plausible given the impedance contrast ( $\approx 4$ ) between the bedrock and the sedimentary basin. This leads to a frequency-dependent factor used to correct the EGF amplitude spectrum. This factor equals 1 above 3 Hz and does not change the vertical component. The EW and NS-component modifications at

1 Hz do not exceed a factor of 5, except for station G15 for which a change in the fault azimuth shifts from a maximum to a node of the  $SH$  radiation pattern, and the EW-component correction factor equals 0.05. The resulting EGF amplitude spectrum modification is large but significantly improves the fit between the 3-D simulation and the EGFs (Fig. 6a).

### EGF uncertainties

The small event input parameters (moment magnitude  $M_w$ , corner frequency  $f_c$  and  $K$  value  $K_s$ ) are only known with large uncertainties. Here we analyse the influence of a potential parameter value misestimation on the simulated ground motion. More precisely, the sensitivity to each EGF parameter is investigated by looking ASTF

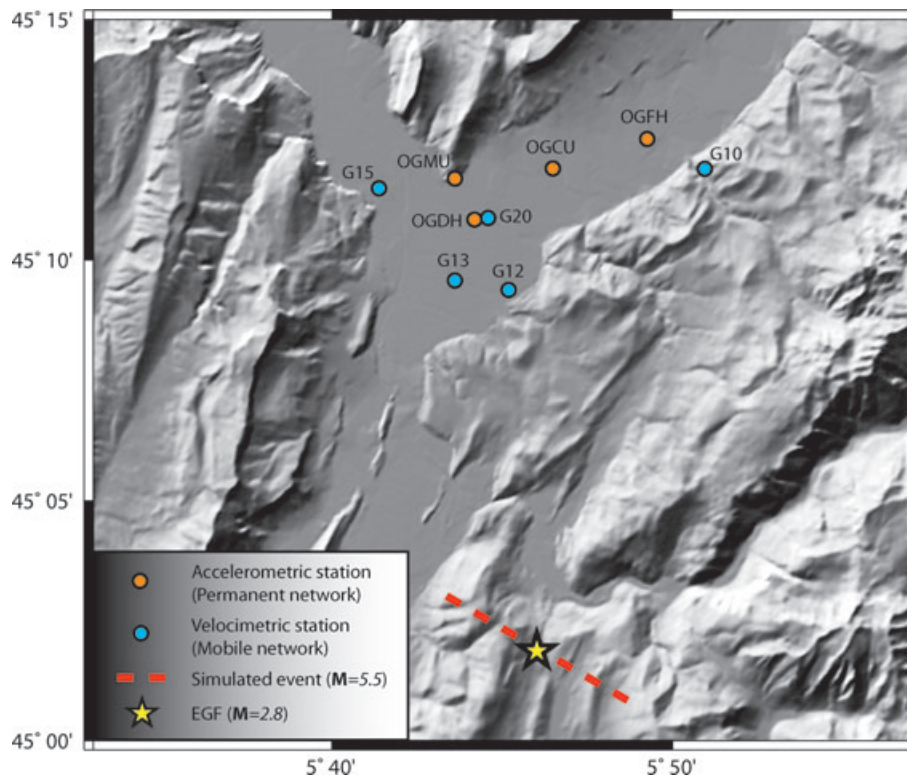


**Figure 5.** Map of the Grenoble valley, station and fault location.

changes when varying the given parameter around its supposed best estimate value, while keeping the other parameters unchanged. First, the  $M_W$  reference value is chosen by assuming  $m_L = M_W$  for small events, which leads to  $M_W = 2.8$ . A deviation of plus or minus 0.2 from the  $M_W$  reference value results in a change of a factor 2 in the seismic moment value  $m_0$ , and consequently, in the number of EGF to sum up. Therefore, the simulations are largely sensitive to the  $M_W$  value at low frequency (Fig. 7a). Furthermore, the corner frequency controls the EGF rupture length  $l$  (eq. 8), and consequently, the target event fault plane dimension. For instance, underestimating the  $f_c$  value leads to increased rupture length  $L$  and decreased target event corner frequency  $f_c$ . Since the number of summed EGF is unchanged, the  $f_c$  uncertainty does not concern the low-frequency and high-frequency expected spectral levels (Fig. 7b). Finally, Fig. 7(c) shows the effects of varying the  $K_s$  value, assuming self-similarity between the small and the target events ( $K = K_s$ ). As  $f_c$  is kept constant, changing  $K_s$  also affects the rupture lengths  $l$  and  $L$ .

In addition, it has been assumed that the small event is not affected by directivity effects. If this hypothesis is rejected, first, the simple correction applied to account for the EGF fault strike modification (initial estimated value of  $160^\circ$  set equal to  $120^\circ$ , see section ‘EGFs’) should also include a modification of  $f_c$ . Nevertheless, the procedure applied in this study to simulate ground motion above  $f_c$  ensure that the expected ASTF spectral level at  $f_c$  is obtained, whatever the  $f_c$  value is. Consequently, the particular EGF directivity effects are not expected to significantly modify the simulation results. Second, although the  $\Theta$  values differ from one station to the other (Fig. 5), the  $f_c$  reference value has been set from the data recorded at OGMU rock station and is supposed to be the same for all the stations. However, the difference in the  $\Theta$  values is not large. Thus, once again, this approximation is expected to bring only minor modifications on ground motion. Using several EGFs would

ensure that the potential small event directivity effects are averaged. However, in moderate seismicity area like the Grenoble basin, very few events are available.

### HGFs

Since the EGFs have a satisfactory signal-to-noise ratio ( $>2$ ) only beyond about 1 Hz, they are not adequate to simulate the low-frequency ground motion. Consequently, low frequencies are computed with the spectral element method (SEM) and combined in the time domain with the EGFs to obtain a set of HGFs (Kamae *et al.* 1998). The SEM is a high-order method that combines the ability of finite element methods to handle 3-D geometries and the minimal numerical dispersion of spectral methods (Komatitsch & Vilotte 1998; Komatitsch & Tromp 1999). The reader is referred to Chaljub *et al.* (2007), Komatitsch *et al.* (2004), Lee *et al.* (2008) and Chaljub (2009) for details about the application of the SEM to ground motion estimation in sedimentary basins or valleys. The SEM is particularly well suited for ground motion estimation in alpine valleys because of its natural ability to account for free-surface topography and its accuracy to model the propagation of surface waves, such as those diffracted off the valley edges. The numerical prediction of ground motion with the SEM presented hereafter have been carefully validated by comparison with those of other advanced 3-D methods, during the numerical benchmark organized within the 2006 symposium on the effects of surface geology (ESG) on ground motion (Chaljub *et al.* 2009; Tsuno *et al.* 2009).

Deterministic ground motion calculations implicitly assume that the 3-D structure (i.e. the positions of the physical interfaces, seismic wave velocities, densities, attenuation factors, etc.) is known from the source region to the receivers. For the Grenoble area, we use a simple 1-D model of the crust combined with a 3-D model

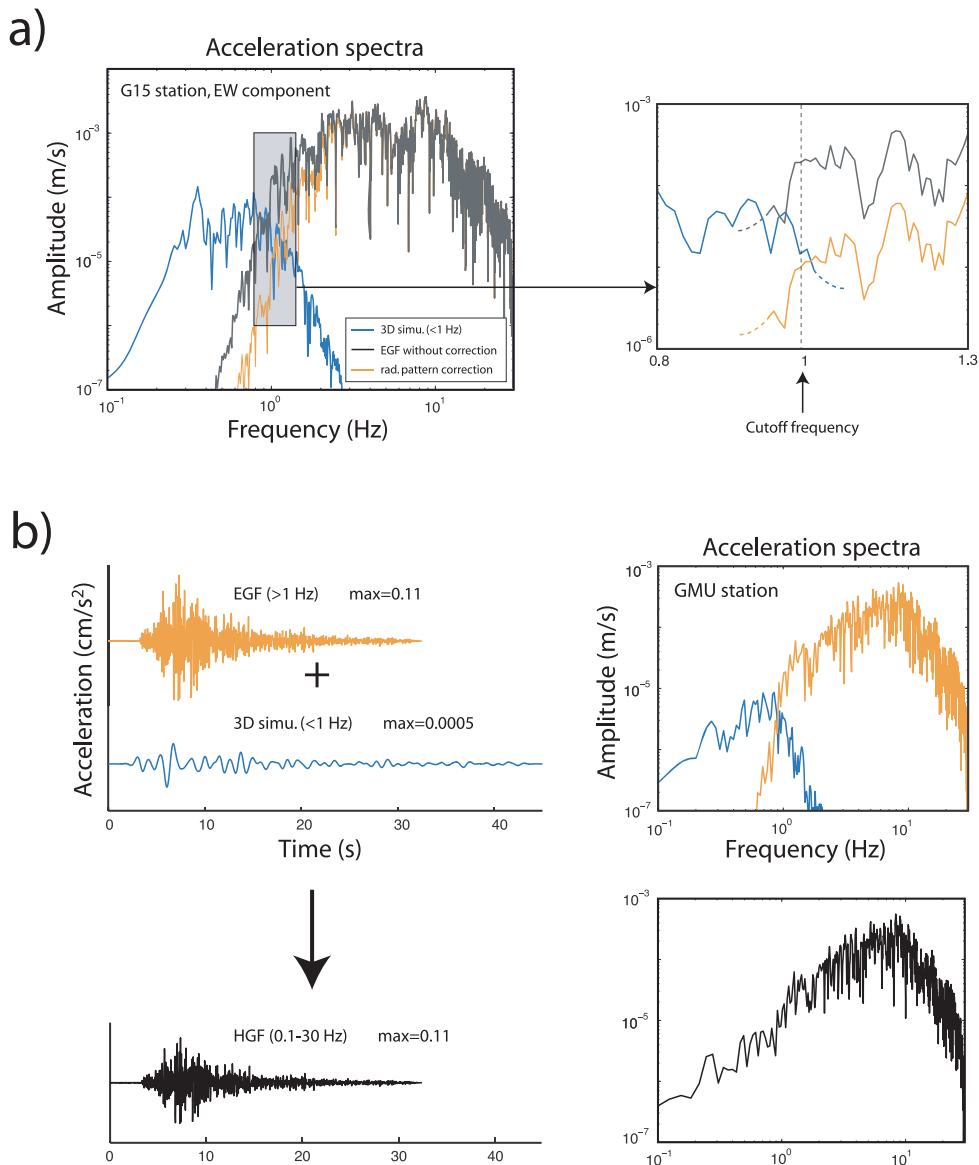


**Figure 6.** (a) Effect of the EGF radiation pattern correction on the fitting between the deterministic and the empirical ground motion. (b) Principle of the low-frequency ground motion simulation. 3D-simulations and EGFs are filtered and summed on each subfault to obtain a set of HGFs.

of the sedimentary valley. The crustal model is defined following Thouvenot *et al.* (2003) and given in Table 2.

The 3-D valley model is bounded by the sediment-bedrock interface obtained by Vallon (1999). Within the sedimentary cover, seismic velocities and densities are only allowed to vary with depth as

$$\begin{cases} a = 300.0 + 19.0 \times \sqrt{d}, \\ b = 1450.0 + 1.2 \times d, \\ \rho = 2140.0 + 0.125 \times d, \end{cases} \quad (13)$$

where depth  $d$  is given in m,  $P$  (resp.  $S$ ) velocities  $a$  (resp.  $b$ ) in  $\text{m s}^{-1}$  and mass density  $\rho$  in  $\text{kg m}^{-3}$ . Finally, we account for attenuation in the sediments by assuming a finite shear quality factor  $Q_\mu = 50$  and an infinite bulk quality factor  $Q_\kappa$ .

The depth dependence of seismic velocities given by eq. (13) relies on direct measurements made for depths larger than 40 m in a deep borehole drilled in 1999 in the eastern part of the valley

(Nicoud *et al.* 2002). It also matches closely the values derived from a refraction profile in the western part of the valley (Cornou 2002; Dietrich *et al.* 2009). This is consistent with the early geological history of the valley since the deep part of the sedimentary cover (i.e. below about  $-30$  m) was formed by the sedimentation of postglacial lacustrine deposits, a smooth process that did not produce strong lateral variations. The shallower part, filled by the deposits of the Isère and Drac rivers, is known to be much more heterogeneous and a continuous effort is deployed to map these lateral variations into a fully 3-D model of the valley. The 1-D model defined by eq. (13) provides a crude average of the shallow subsurface but it has been shown to explain reasonably well the ground motion characteristics for frequencies below 1.5 Hz, in particular the level of amplification between bedrock and sediments (Chaljub *et al.* 2004, 2005; Chaljub 2009) and the ambient noise propagation properties (Cornou *et al.* 2008).

In order to define the low frequency part of the HGFs, we need to compute the ground motion at a small number of stations (9 for

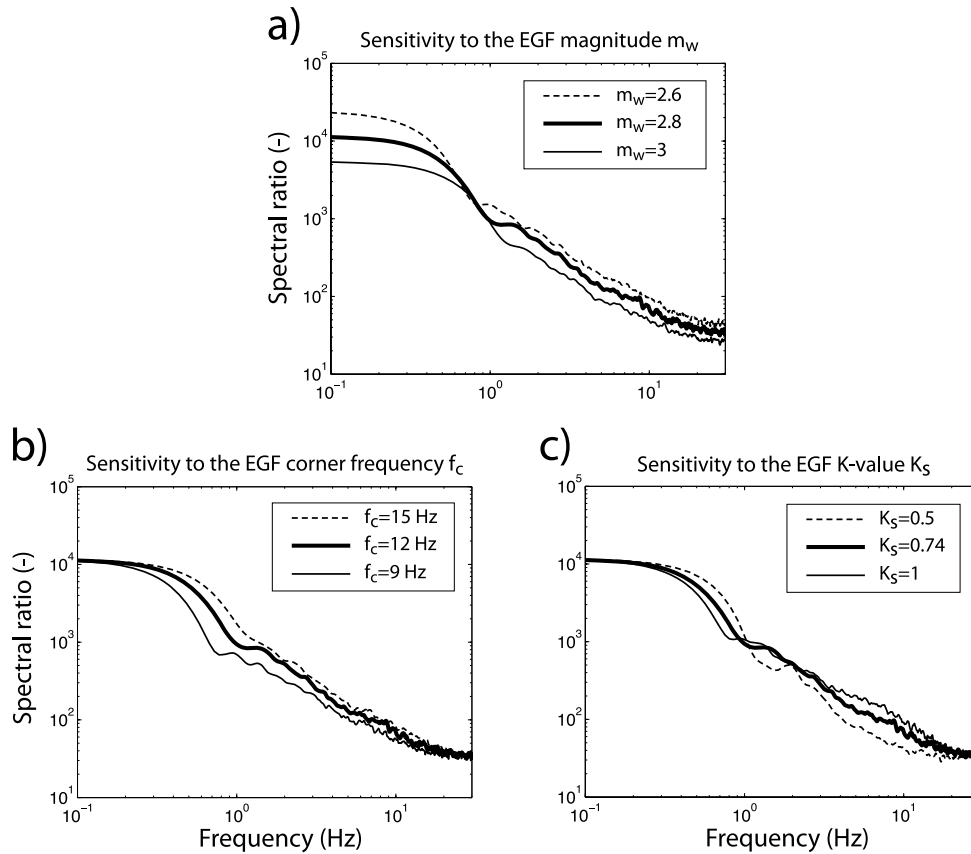


**Figure 7.** Sensitivity of the ASTF to the EGF parameters  $M_W$ ,  $f_c$  and  $K_S$ . The assumed reference values are  $M_W = 2.8$ ,  $f_c = 12$  Hz and  $K_S = 0.74$ . The spectra correspond to the quadratic mean of 100 simulated spectra for  $\Theta = 90^\circ$  and  $\tau_{\max} = 0.6$  s.

**Table 2.** 1-D velocity and density model of the bedrock used for estimating the deterministic part of the hybrid Green's functions.

Depth of top layer (km)	$\alpha$ (km s $^{-1}$ )	$\beta$ (km s $^{-1}$ )	$\rho$ (g cm $^{-3}$ )	Quality factor
0	5.60	3.20	2.72	$\infty$
3	5.92	3.43	2.72	$\infty$
27	6.60	3.81	2.92	$\infty$
35	8.00	4.45	3.32	$\infty$

the results presented in this paper) due to a large number of point sources distributed on the fault plane. The fault plane is discretized into  $36 \times 18 = 648$  square subfaults of length 160 m. It is therefore indicated to invoke the reciprocity of the wave equation and to switch the respective roles of sources and receivers, as suggested by Eisner & Clayton (2001), Graves & Wald (2001) and recently implemented by Zhao *et al.* (2006) for tomographic applications.

Let  $\mathbf{x}^R$  stand for the position of one of the receivers. The  $i$ th component of the displacement field due to a double-couple punctual source located at  $\mathbf{x}^S$  is

$$u_i(\mathbf{x}^R, t) = \frac{\partial G_{ji}}{\partial x_k^S}(\mathbf{x}^R, \mathbf{x}^S, t) * M_{jk}(\mathbf{x}^S, t), \quad (14)$$

where  $G$  is the Green's function and  $M$  gathers the seismic moment tensor and the source time function. Note that  $G$  has to be evaluated at the receiver position. Applying reciprocity yields

$$u_i(\mathbf{x}^R, t) = \frac{\partial G_{ij}}{\partial x_k^S}(\mathbf{x}^S, \mathbf{x}^R, t) * M_{jk}(\mathbf{x}^S, t), \quad (15)$$

where now the Green's function is the displacement field evaluated at the source position due to a unit force located at the receiver. The final seismic moment is described with a Heaviside function, scaled to the EGF magnitude ( $M_L = 2.8$ ).

Following eq. (15), we thus performed a total of 27 simulations, 3 unit forces in the  $x$ ,  $y$  and  $z$  directions for each of the nine receivers, and recorded the spatial derivatives of the ground displacement at the 648 points defining the fault plane. The grid used for those calculations contains about 40 000 elements (2 600 000 points) and provides a sampling of at least five gridpoints per wavelength for frequencies up to 2 Hz. The computation of 90 s of these 157 464 derivatives of Green's functions required a continuous access to 32 CPUs during about 2 months.

Next, both deterministic and empirical parts of the Green's functions are summed in the time domain on each subfault by adjusting the  $P$ -waves arrival times (Fig. 6b). Numerical simulations and EGFs are, respectively, low-passed and high-passed filtered with a pair of complementary filters. A set of 648 three-component HFG is obtained for each station. Given that the EGFs do not have a satisfactory signal-to-noise ratio below 1 Hz and that deterministic Green's functions are calculated up to 2 Hz, the value of the filter cut-off frequency can be chosen within this range. Numerical simulations result in a set of Green's functions specific to the subfault-receiver path. This is not the case for the empirical part since the same EGF is used for each part of the fault plane. Nevertheless, the numerical simulation accuracy is strongly limited by the lack of detailed knowledge of the propagation medium. Therefore, the cut-off frequency is chosen to be 1 Hz (Fig. 6b).

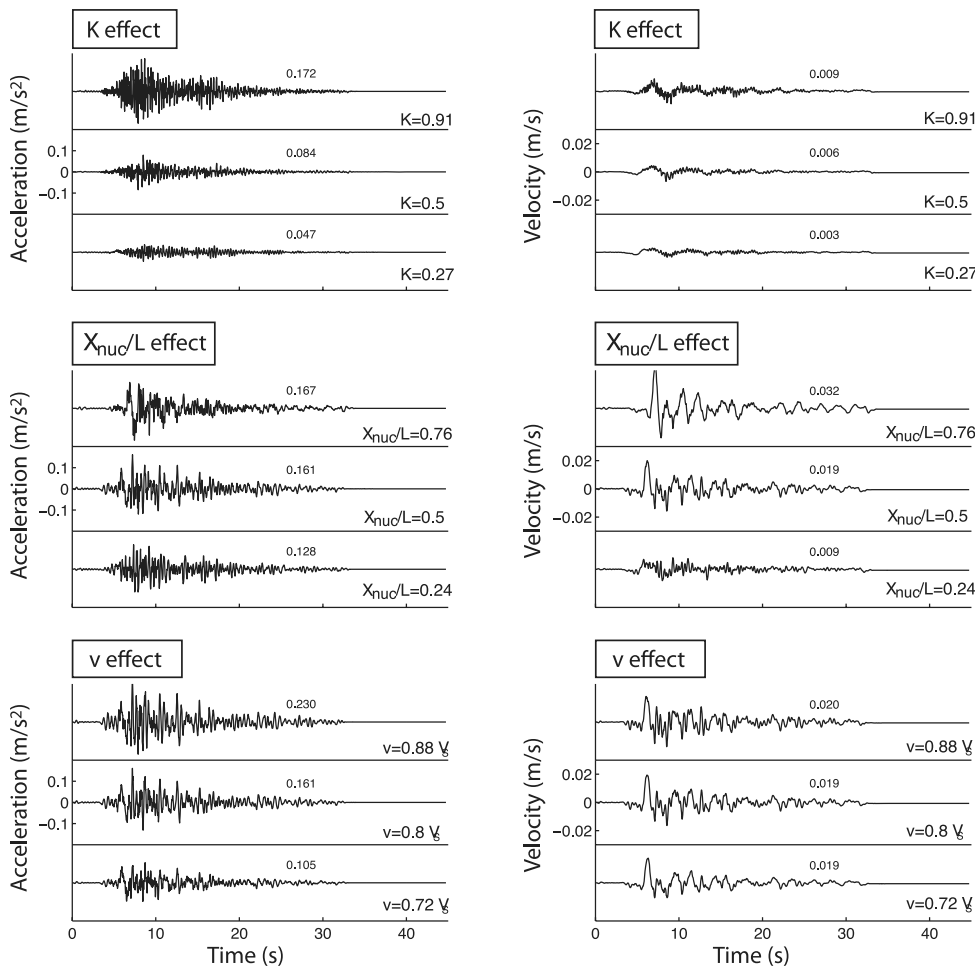


**Figure 8.** Sensitivity of the ground acceleration with respect to the variation by one standard deviation of the parameter  $K$ , the hypocentre abscissa  $X_{\text{nuc}}$  and the rupture velocity  $v$ . Acceleration and velocity time histories are the EW-components at station OGMU. The maximum value is indicated on the right of each time-series.  $X_{\text{nuc}}/L \leq 0.5$  corresponds to the northwestern part of the fault. In order to show the  $K$  effects, an antidirective unilateral rupture is supposed. This way the sensitivity to  $K$  can be observed not only on the ground acceleration but also on the velocity. To study the  $v$  effects, the hypocentre is set on the middle of the fault.

## GROUND MOTION PREDICTIONS

### Ground motion variability assessment

The ground motion prediction variability is evaluated by first defining the source parameter uncertainties and then calculating their effects on the SA. More precisely the  $k^{-2}$  model parameters are assigned probability density functions. The Latine hypercube sampling (LHS) method (McKay 1988) is next applied to select for each parameter a set of  $n$  values, chosen with respect to its distribution. These values are randomly combined for obtaining a set of  $n$  samples of source parameters (see Pavic *et al.* 2000, for more details). Finally, the resulting parameter combinations are used to simulate, with the aforementioned summation algorithm, a class of  $n$  response spectra, from which the median and standard deviation of SA are calculated. In this study, a value of  $n = 50$  is taken. For each simulation the high wavenumber slip spectrum phases are randomly defined.

The source parameter distributions are assessed by investigating their scattering obtained from past kinematic inversion studies. Mai *et al.* (2005) have analysed the hypocentre position by studying a database of more than 80 finite-source rupture models and defined probability density functions that we used in this paper. Somerville

*et al.* (1999) also detailed the characteristics of 15 crustal earthquake slip models, from which they derived a relation between the corner wavenumber  $k_c = K/L$  and the seismic moment. For a  $M_W$  5.5 event, the relation gives a median  $K$  value of 0.5 with a standard error of 0.26. Taking this distribution, the  $n = 50$   $K$ -values range from 0.17 to 1.2. Consequently, according to the discussion of Appendix A, the slip model correction proposed to remove the negative slip areas can be applied. Next we supposed that the rupture velocity  $v$  is uniformly distributed between  $0.7c$  and  $0.9c$ , where  $c$  is the shear wave velocity. Finally, we assume a constant rise-time  $\tau_{\text{max}}$  equal to 0.25 s, which is the average value proposed by Somerville *et al.* (1999) for a  $M_W$  5.5 earthquake. Fig. 8 displays the effects of the source parameters uncertainties on the ground acceleration and velocity at rock station OGMU. Are also shown examples of amplitude acceleration Fourier spectra for unilateral directive and antidirective ruptures (Fig. 9).

### Simulation on rock and validation

In order to test the reliability of the ground motion predictions, simulations on rock site are compared to the empirical ground motions equations of Bragato & Slejko (2005) and to the stochastic

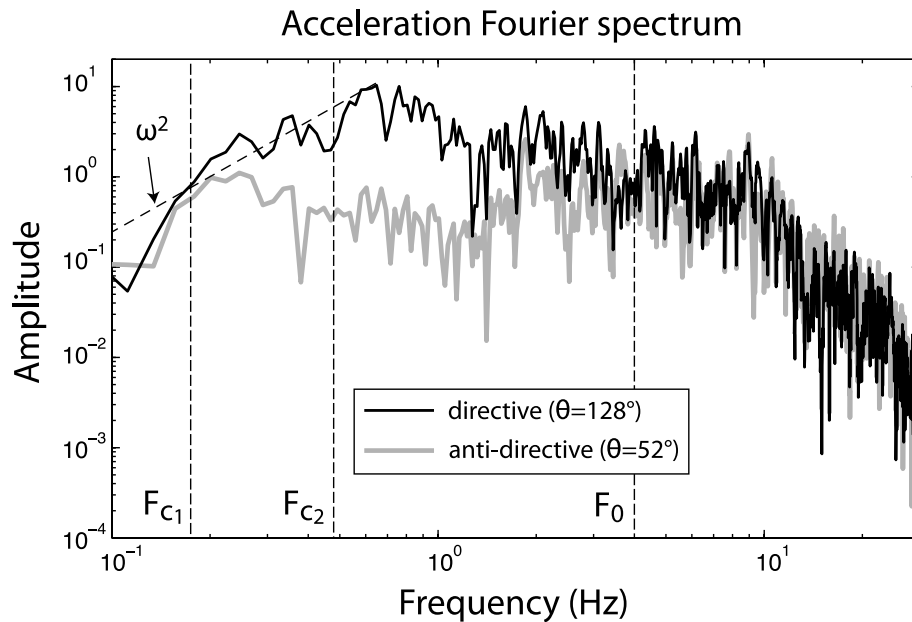


**Figure 9.** Example of amplitude acceleration Fourier spectra for unilateral directive and antidirective ruptures, at OGMU rock station (EW component). The slope is approximately  $\omega^2$  below  $F_{c1}$  and  $F_{c2}$  (theoretical corner frequency values for a non-directive and a directive propagation, respectively). The spectral level is flat and equal for both rupture types beyond the transition frequency  $F_0$ , and starts decreasing above about 10 Hz, due to the seismic wave attenuation.

method developed by Pousse *et al.* (2006). Both methods, based on real data, provide estimation of the ground motion median and standard deviation expected at a rock station. Bragato & Slejko (2005) empirical equations have been derived from a large data set of seismometric and accelerometric records collected in the Eastern Alps and are valid in the magnitude range 2.5–6.3 for distances of up to 130 km. Pousse *et al.* (2006) method generates time-domain accelerograms following a specific time envelope and based on the assumption that phases are random. The frequency content of the signal follows a modified  $\omega^{-2}$  model. The method depends on four indicators (peak ground acceleration, strong-motion duration, Arias intensity and central frequency), empirically connected to Japanese data recorded by the K-net array.

Fig. 10 stands for the comparison between the EGF response spectra at rock stations (OGMU and G10) and Bragato & Slejko (2005) predictions. The good agreement between the data and Bragato & Slejko (2005) model in the frequency range 0.5–3 Hz, especially for station G10, shows that the EGF seismic moment estimation is correct. Discrepancies observed at frequencies above 3 Hz can be explained by the rock stiffness differences at stations OGMU and G10.  $V_{S30}$  is close to 2200  $\text{m s}^{-1}$  at OGMU and 1500  $\text{m s}^{-1}$  at G10, whereas Bragato & Slejko (2005) model includes softer rock types ( $800 < V_{S30} < 1500 \text{ m s}^{-1}$  on average; P. L. Bragato, 2008, personal communication). In the following station G10, which best fits the empirical model rock site definition, is kept as the reference rock station.

Comparison between our  $k^{-2}$  hybrid calculations, Bragato & Slejko (2005) predictions and Pousse *et al.* (2006) stochastic simulations is displayed on Fig. 11. Stochastic simulations are initially adjusted to adapt the definition of rock. Indeed the K-net array rock types used in Pousse *et al.* (2006) correspond to  $V_{S30} \approx 800 \text{ m s}^{-1}$ . Pousse *et al.* (2006)  $V_{S30}$  is thus set equal to 1500  $\text{m s}^{-1}$ . Since the roughness parameter  $K$  median value is poorly constrained by Somerville *et al.* (1999) empirical model, ground motion predictions are shown not only for a median value  $K = 0.5$  but also for

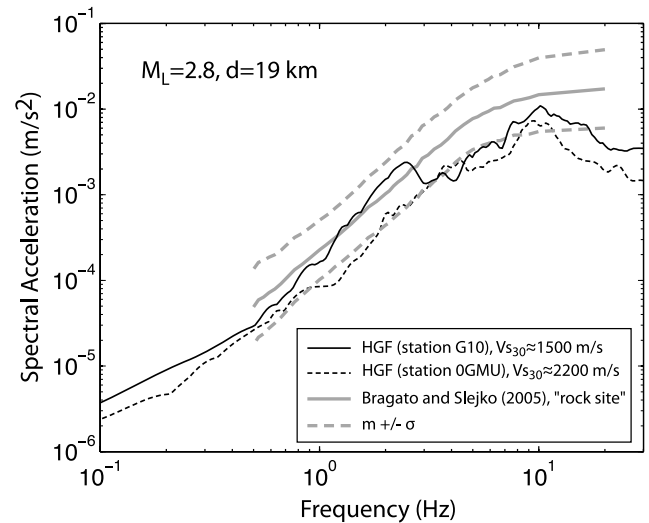


**Figure 10.** Comparison between the EGF response spectra at rock stations OGMU and G10 (EW component) and Bragato & Slejko (2005) empirical ground motion equations for a rock site,  $M_L = 2.8$  and an epicentral distance equal to 19 km.

$K = K_S = 0.74$  (self-similarity between the small and the simulated events) and for  $K = 1$  [value used in the classical model of Herrero & Bernard (1994)]. First, for  $K = 0.5$ , our ground motion simulations well match Bragato & Slejko (2005) empirical equations in the frequency range 0.5–2 Hz and predict lower values for higher frequencies (Fig. 11a). This is consistent with the comparison between the EGF and the empirical equation predictions, showing a similar tendency (Fig. 10). The difference observed at high frequency decreases with an increasing  $K$  value. Second, a value of  $K = 1$  is necessary to improve the agreement between  $k^{-2}$  hybrid simulations and Pousse *et al.* (2006) corrected response spectra. For

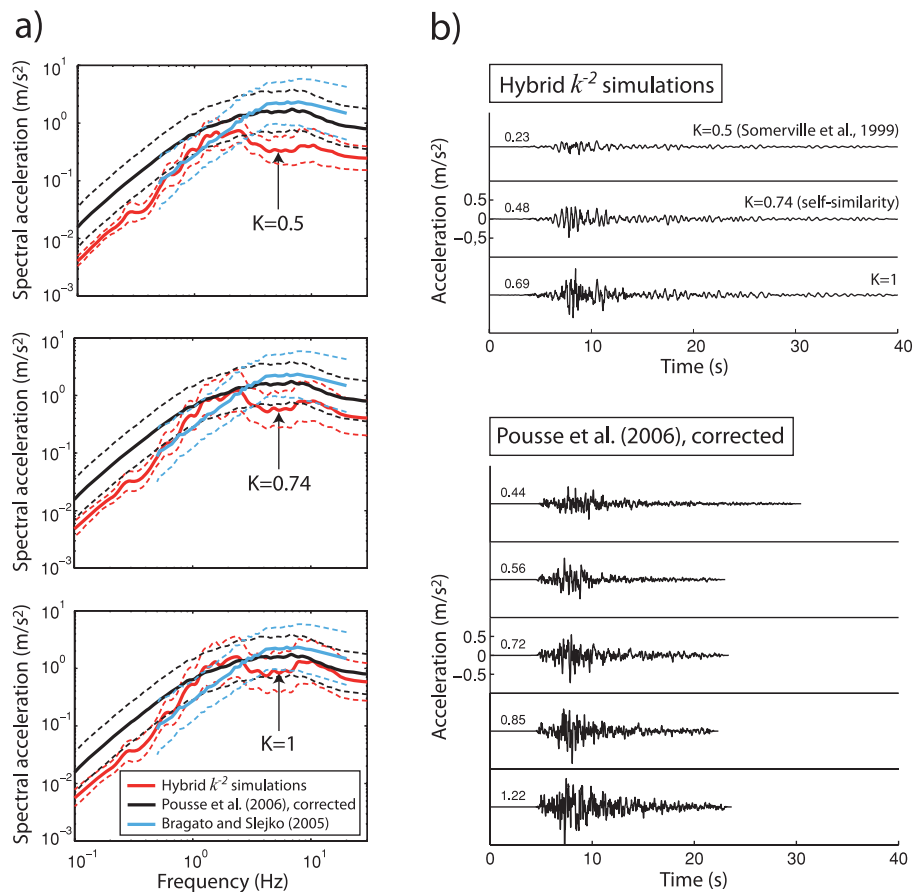


**Figure 11.** (a) Comparison between the response spectra obtained from our  $k^{-2}$  hybrid predictions (station G10, EW component), Bragato & Slejko (2005) empirical ground motion equations and Pousse *et al.* (2006) stochastic simulations, corrected according to Cotton *et al.* (2006) procedure ( $V_{S30} = 1500 \text{ m s}^{-1}$ ). The dashed line correspond to the plus and minus standard deviation spectra. (b) Example of accelerograms (station G10, EW component) obtained from the  $k^{-2}$  hybrid procedure. Are also shown example of Pousse *et al.* (2006) corrected stochastic simulations. The six time-series span the median ground motion within  $\pm 1 \text{ SD}$ .

$K = 1$ , the obtained time-series are also similar in terms of amplitude and duration (Fig. 11b). Note that below 1 Hz, the stochastic simulations exceed the other predictions of a factor of about 2. This difference may come from Pousse *et al.* (2006) procedure, that overestimates the acceleration Fourier amplitude below the corner frequency for moderate sized earthquakes (Fabian Bonilla, 2008, personal communication—see also fig. 8 of Pousse *et al.* 2006).

Despite the discrepancies observed at high frequency, one can conclude that our simulations are consistent with Bragato & Slejko (2005) empirical equations and the stochastic simulations, for the three tested  $K$  values.

### Simulation on sediment

In order to simulate ground motion at sediment stations, a  $K$  value of 0.5 is kept, since it results from past earthquake analysis (Somerville *et al.* 1999, relationships). The comparison at the rock station G10 with Bragato & Slejko (2005) empirical equation results and Pousse *et al.* (2006) corrected simulations suggests that  $K = 0.5$  does not lead to overestimated ground motion. Fig. 12 displays the accelerograms derived from median source parameter values at the 9 stations and Fig. 13 displays median and standard deviation of the simulated response spectra. The spectra are compared with the European regulation spectra (EC8) for rock site (category A in EC8 classification)

or for standard to stiff soils (category B and C) for the stations located within the basin. First, our predictions exceed the EC8 spectra at some sites and some frequencies, especially at station OGDH, which exhibits two peaks at 0.3 and 2 Hz. The first peak, generated by 3-D simulations ( $< 1 \text{ Hz}$ ), corresponds to the fundamental resonance frequency of the sedimentary basin (Lebrun *et al.* 2001; Guéguen *et al.* 2006a). This peak also clearly appears at stations OGFH, G15 and G20. This confirms the importance of coupling the EGF with 3-D numerical calculations. The second peak at 2 Hz has been well identified from geophysical and geotechnical surveys (Guéguen *et al.* 2006b, P. Guéguen and S. Garambois, unpublished manuscript) and from global inversion methods (Drouet *et al.* 2007). This is interpreted as the resonance effects within a surficial soft clay layer overlaying more competent sandy graver layers. Second, the spectral responses at stations G20 and OGDH, located only a few hundreds of meters away, obviously diverge beyond 1 Hz. This points out the large spatial variability of the high-frequency amplification effects, caused by fast lateral variations of the upper soft sediment layers (Tsunoi *et al.* 2008). Such variations are observed from several drillings and surface wave measurements performed in this area. Third, the EC8 design spectra largely exceed our simulations at rock stations OGMU and G10. These results indicate that standard European regulations provide a frequency-dependent and site-dependent safety margin in the Grenoble basin. The use of HGFs suggests the need of specific design spectra in Grenoble,

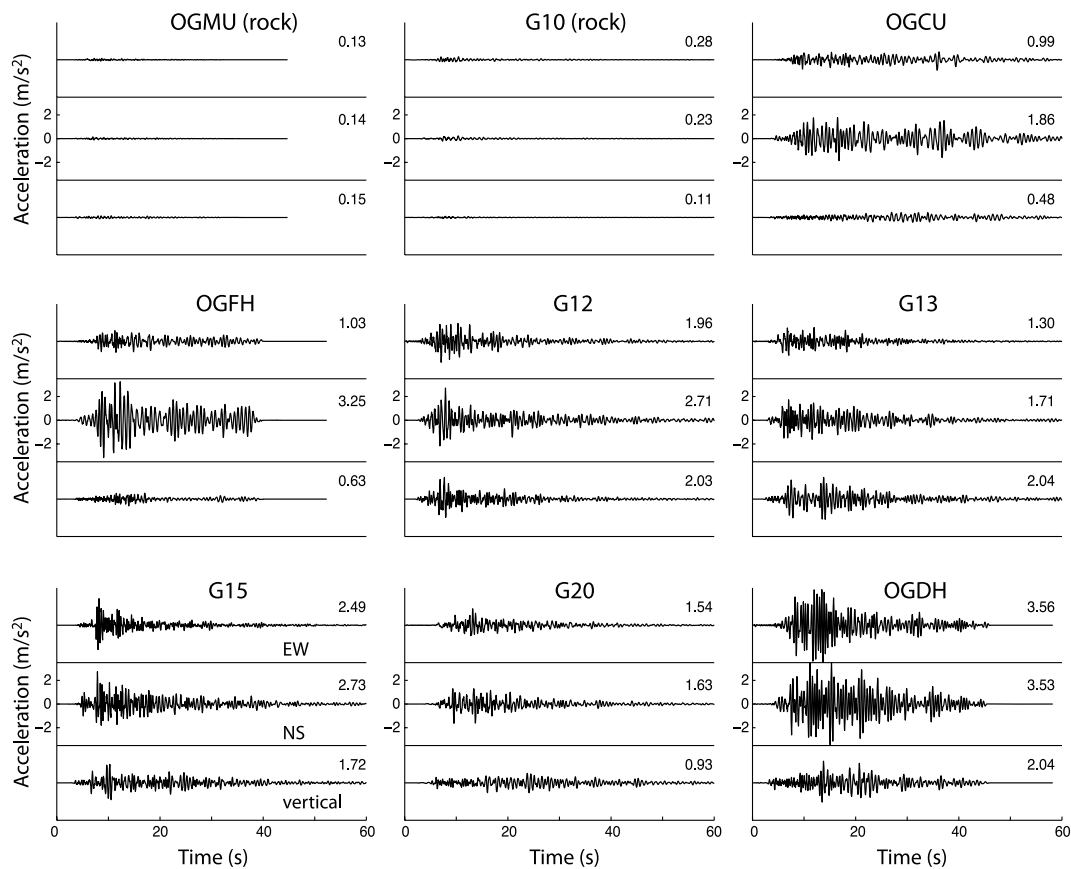


**Figure 12.** Simulated accelerograms for median parameter values. The maximum value is indicated on the right of each accelerogram.

with increased low-frequency level in the valley and much smaller spectra on rock. Microzonation studies are thus preferable in such a specific geological context.

## CONCLUSION

A new method has been introduced for performing broad-band ground motion time histories from a finite-extent source model. This method includes specific site effects and is adequate for simulating ground motion in 3-D deep alluvial valleys. The ground acceleration is computed in the frequency range 0.1–30 Hz with a new approach coupling  $k^{-2}$  source model and HGFs, obtained by summing reciprocity-based SEM 3-D simulations (<1 Hz) and EGFs. A procedure is proposed to assess the ground motion prediction variability due to the source rupture process, from specific distributions of the  $k^{-2}$  model parameters. We used this new approach for predicting ground motion for a potential  $M_w$  5.5 earthquake in the Grenoble valley. At sediment sites, the simulated response spectra significantly differ from one station to the other. At some sites simulations present large response spectra both at high-frequency (>1 Hz) and low-frequency ( $\approx 0.3$  Hz) and EC8 spectra are exceeded. This points out the interest of coupling EGFs and 3-D numerical simulations in such deep valleys.

The method presented relies on reliable estimation of the source model parameter distributions. Our ground motion estimations especially depends on the slip distribution roughness, controlled by the parameter  $K$ . In order to estimate the *a priori*  $K$  value distribution, Somerville *et al.* (1999) scaling laws have been used. Neverthe-

less, the reliability of these relationships may be questionable. First, Somerville *et al.* (1999) results have been derived from a small number of inverted source models (15) and the event magnitudes  $M_w$  range from 5.6 to 7.2, which decreases the  $K$  estimation robustness for a  $M_w$  5.5 event. Second, the inverse problem parametrization often involves subjective decision resulting in highly different inverted slip images and there is no basis to distinguish between artefacts, smoothing constraints and real features (Beresnev 2003). The comparison made in Fig. 11 indicates that a median  $K$  value of 0.5 may result in underestimated ground motion. There is thus a need of improving earthquake model databases to better constrain source parameters for performing blind predictions. An other approach would have been to set the median  $K$  value equal to 1, which leads to the best fit between the predictions at rock station G10, Bragato & Slejko (2005) predictions and Pousse *et al.* (2006) corrected simulations. Such a calibration is also proposed by Causse *et al.* (2008). Nevertheless, this approach would not change the general conclusion on the comparison between the ground motion predictions at sediment stations and the EC8 design spectra.

## ACKNOWLEDGMENTS

Mathieu Causse's grant is funded by CEA and CNRS. This work benefits from ANR-QSHA and SIRSEG(MEDAD) programs. Fabrice Cotton's work is supported by Institut Universitaire de France. All the computations presented in this paper were performed at the Service Commun de Calcul Intensif de l'Observatoire de Grenoble (SCCI). The authors would also like to thank the French

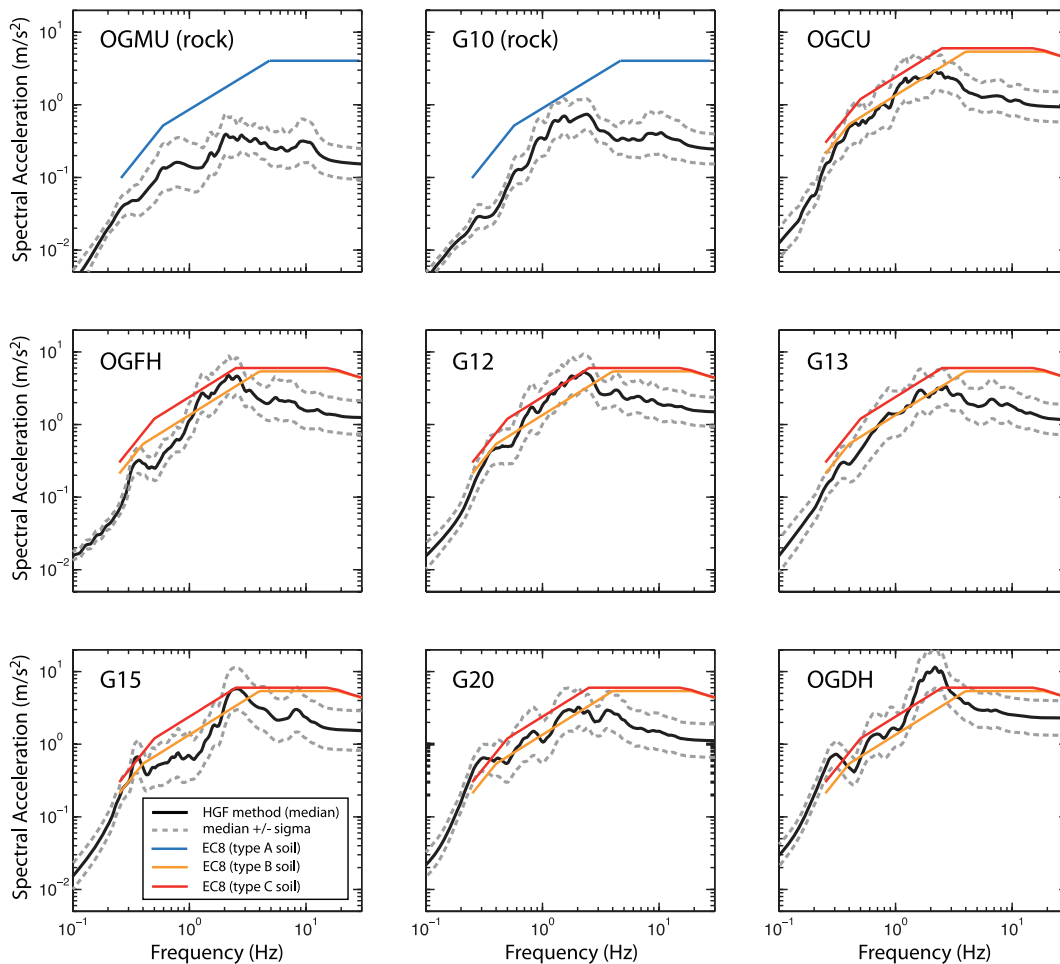


**Figure 13.** Simulated median and standard deviation of the spectral acceleration (EW component), compared with EC8 spectra. The median  $K$  value is  $K = 0.5$ , as suggested by Somerville *et al.* (1999) empirical model.

Accelerometric Permanent network and all the participants to the 2005 Grenoble experiment (Chaljub *et al.* 2006).

## REFERENCES

- Aki, K. & Richards, P.G., 2002. *Quantitative Seismology*, 2nd edn., University Science Books, Sausalito, CA.
- Ben-Menahem, A., 1961. Radiation of seismic surface-waves from finite moving sources, *Bull. seism. Soc. Am.*, **51**, 401–435.
- Beresnev, I.A., 2003. Uncertainties in finite-fault slip inversions: to what extent to believe? A critical review, *Bull. seism. Soc. Am.*, **93**, 2445–2458.
- Bernard, P. & Herrero, A., 1994. Slip heterogeneity, body-wave spectra, and directivity of earthquake ruptures, *Annali Di Geofisica*, **XXXVII**, 1679–1690.
- Bernard, P., Herrero, A. & Berge C., 1996. Modeling directivity of heterogeneous earthquake ruptures, *Bull. seism. Soc. Am.*, **86**, 1149–1160.
- Boatwright, J., 2007. The persistence of directivity in small earthquakes, *Bull. seism. Soc. Am.*, **97**, 1850–1861.
- Bour, M. & Cara, M., 1997. Test of a simple empirical Green's function method on moderate-sized earthquakes, *Bull. seism. Soc. Am.*, **87**, 668–683.
- Bragato, P.L. & Slejko, D., 2005. Empirical ground motion attenuation relations for the eastern Alps in the magnitude range 2.5–6.3, *Bull. seism. Soc. Am.*, **95**, 252–276.
- Brune, J.N., 1970. Tectonic stress and the spectra of seismic shear waves from earthquakes, *J. geophys. Res.*, **75**, 4997–5009.
- Causse, M., Cotton, F., Cornou, C. & Bard P.-Y., 2008. Calibrating median and uncertainties estimates for a practical use of EGF technique, *Bull. seism. Soc. Am.*, **98**, 344–353.
- Chaljub, E., 2009. Spectral element modeling of 3D wave propagation in the alpine valley of Grenoble, France, in *Third International Symposium on the Effects of Surface Geology on Seismic Motion*, Vol. 2, pp. 1467–1474, eds Bard, P.Y., Chaljub, E., Cornou, C., Cotton, F. & Guéguen, P., LCPC Editions.
- Chaljub, E., Cornou, C., Guéguen, P., Causse, M. & Komatitsch, D., 2004. Spectral element modeling of 3D site effects in the alpine valley of Grenoble, France, in *Fall Meet. Suppl., Abstract S41C-07, EOS, Trans. Am. Geophys. Un.* **85**(47).
- Chaljub, E., Cornou, C., Guéguen, P., Causse, M. & Komatitsch, D., 2005. Spectral-element modeling of 3D wave propagation in the alpine valley of Grenoble, France, in *Geophysical Research Abstracts*, Vol. 7, 05225. EGU 2nd General Assembly, Wien, Austria.
- Chaljub, E. *et al.*, 2006. Measurement and variability study of site effects in the 3D glacial valley of Grenoble, French Alps, in LCPC Editions, editor, *Proceeding of the Third International Symposium on the Effects of Surface Geology on Seismic Motion*, number 154, Grenoble, France.
- Chaljub, E., Komatitsch, D., Vilotte, J.P., Capdeville, Y., Valette, B. & Festa, G., 2007. Spectral element analysis in seismology, in *Advances in Wave Propagation in Heterogeneous Media*, Vol. 48, pp. 365–419, eds Wu, R. & Maupin, V., Advances in Geophysics, Elsevier - Academic Press.
- Chaljub, E., Cornou, C. & Bard, P.Y., 2009. Numerical benchmark of 3D ground motion simulation in the valley of Grenoble, France, in *Third International Symposium on the Effects of Surface Geology on Seismic*

- Motion, Vol. 2, pp. 1365–1376, eds Bard, P.Y., Chaljub, E., Cornou, C., Cotton, F. & Guéguen, P., LCPC Editions.
- Cornou, C., 2002. Traitement d'antenne et imagerie sismique dans l'agglomération grenobloise (Alpes françaises): implications pour les effets de site, *PhD thesis*, Université Joseph Fourier, Grenoble I.
- Cornou, C., Bard, P.Y. & Dietrich, M., 2003. Contribution of dense array analysis to basin-edge-induced waves identification and quantification. application to grenoble basin, french Alps (ii), *Bull. seism. Soc. Am.*, **93**, 2624–2648.
- Cornou, C., Tsuno, S. & Chaljub, E., 2008. Real and synthetic ambient noise recordings in the Grenoble basin: reliability of the 3D numerical model, in *The 14th World Conference on Earthquake Engineering*, Beijing, China.
- Cotton, F., Scherbaum, F., Bommer, J., Bungum, H. & Sabetta, F., 2006. Criteria for selecting and adapting ground motion models for specific target region. Application to Central Europe and rock sites, *J. Seism.*, **1**, 1–20.
- Dietrich, M., Cornou, C., Ménard, G., Lemeille, F., Guyoton, F. & Guiguet, R., 2009. Seismic profiling and borehole measurements in the Isère valley near Grenoble, France—1: data acquisition and processing, in *Third International Symposium on the Effects of Surface Geology on Seismic Motion*, Vol. 2, pp. 1597–1608, eds Bard, P.Y., Chaljub, E., Cornou, C., Cotton, F. & Guéguen, P., LCPC Editions.
- Drouet, S., Scherbaum, F., Cotton, F. & Souriau, A., 2007. A selection and ranking of ground motion models for seismic hazard analysis in the Pyrenees, *J. Seism.*, **11**, doi:10.1007/s10950-006-9039-6.
- Eisner, L. & Clayton, R.W., 2001. A reciprocity method for multiple-source simulations, *Bull. seism. Soc. Am.*, **91**, 553–560.
- Galovic, F. & Brokesova, J., 2004. On strong ground motion synthesis with the  $k^{-2}$  slip distribution, *J. Seism.*, **8**, 211–224.
- Gallovic, F. & Burjanek, J., 2007. High frequency directivity in strong ground motion modeling methods, *Ann. Geophys.*, **50**, 203–211.
- Graves, R.W. & Wald, D.J., 2001. Resolution analysis of finite fault source inversion using one- and three-dimensional Green's functions. 1. Strong motions, *J. geophys. Res.*, **106**, 8745–8766.
- Guéguen, P., Cornou, C., Garambois, S. & Banton, J., 2006a. On the limitation of the H/V spectral ratio using seismic noise as an exploration tool: application to the Grenoble valley (France), a small apex ratio basin, *Pure appl. Geophys.*, **164**, 1–20.
- Guéguen, P., Garambois, S., Tadenuma, S., Lebrun, B. & Cotton, F. 2006b. Geotechnical, geophysical and seismological data used for the estimate of the highest amplified frequency in the basin of Grenoble, in *Proceeding of the Third International Symposium on the Effects of Surface Geology on Seismic Motion*, number 100, Grenoble, France.
- Hartzell, S.H., 1978. Earthquakes aftershocks as Green's functions, *Geophys. Res. Lett.*, **5**, 1–4.
- Hartzell, S.H., Guatterri, M., Mai, P.M., Liu, P.C. & Fisk, M., 2005. Calculation of broadband time histories of ground motion, part II: kinematic and dynamic modeling using theoretical Green's functions and comparison with the 1994 Northridge earthquake, *Bull. seism. Soc. Am.*, **95**, 614–645.
- Herrero, A. & Bernard, P., 1994. A kinematic self-similar rupture process for earthquakes, *Bull. seism. Soc. Am.*, **84**, 1216–1228.
- Kamae, K., Irikura, K. & Pitarka, A., 1998. A technique for simulating strong ground motion using hybrid Green's functions, *Bull. seism. Soc. Am.*, **88**, 357–367.
- Kanamori, H. & Anderson, D.L., 1975. Theoretical basis of some empirical relations in seismology, *Bull. seism. Soc. Am.*, **65**, 1073–1095.
- Kohrs-Sansorny, C., Courboulex, F., Bour, M. & Deschamps, A., 2005. A two-stages method for strong ground motions simulations using stochastic summation of small earthquakes, *Bull. seism. Soc. Am.*, **94**, 314–319.
- Komatitsch, D. & Tromp, J., 1999. Introduction to the spectral-element method for three-dimensional seismic wave propagation, *Geophys. J. Int.*, **139**, 806–822.
- Komatitsch, D. & Vilotte, J.P., 1998. The spectral-element method: an efficient tool to simulate the seismic response of 2D and 3D geological structures, *Bull. seism. Soc. Am.*, **88**, 368–392.
- Komatitsch, D., Liu, Q., Tromp, J., Süß, P., Stidham, C. & Shaw, J.H., 2004. Simulations of strong ground motion in the Los Angeles basin based upon the spectral-element method, *Bull. seism. Soc. Am.*, **94**, 187–206.
- Lebrun, B., Hatzfeld, D. & Bard, P.Y., 2001. Site effects study in urban area: experimental results in Grenoble, *Pure appl. Geophys.*, **158**, 2543–2557.
- Lee, S.J., Chen, H.W., Liu, Q., Komatitsch, D., Huang, B.S. & Tromp, J., 2008. Three-dimensional simulations of seismic-wave propagation in the Taipei basin with realistic topography based upon the spectral-element method, *Bull. seism. Soc. Am.*, **98**(1), 99999998–99999999. doi:10.1785/0120070033.
- Mai, P.M., Spudich, P. & Boatwright, J., 2005. Hypocenter locations in finite-source rupture models, *Bull. seism. Soc. Am.*, **95**, 965–980.
- McKay, M.D., 1988. Sensitivity and uncertainty analysis using a statistical sample of input values, in *Uncertainty Analysis*, pp. 145–186, ed. Ronen, Y., CRC Press, Boca Raton, Florida.
- Nicoud, G., Royer, G., Corbin, J.-C., Lemeille, F. & Paillet, A., 2002. Creusement et remplissage de la vallée de l'Isère au Quaternaire récent. Apports nouveaux du forage GMB1 (1999) dans la région de Grenoble (France), *Géologie de la France*, **4**, 39–49, in French.
- Pacor, F., Cultrera, G., Mendez, A. & Cocco, M., 2005. Finite fault modeling of strong ground motions using a hybrid deterministic-stochastic approach, *Bull. seism. Soc. Am.*, **95**, 225–240.
- Pavic, R., Koller, M.G., Bard, P.-Y. & Lacave-Lachet, C., 2000. Ground motion prediction with the empirical Green's function technique: an assessment of uncertainties and confidence level, *J. Seism.*, **4**, 59–77.
- Pousse, G., Bonilla, L.F., Cotton, F. & Margerin, L., 2006. Nonstationary stochastic simulation of strong ground motion time histories including natural variability: application to the K-net Japanese database, *Bull. seism. Soc. Am.*, **96**, 2103–2117.
- Pulido, N. & Kubo, T., 2004. Near-fault strong motion complexity of the 2000 Tottori earthquake (Japan) from a broadband source asperity model, *Tectonophysics*, **390**, 177–192.
- Ruiz, J., Baumont, D., Bernard, P. & Berge-Thierry, C., 2007. New approach in the kinematic  $k^{-2}$  source model for generating physical slip velocity functions, *Geophys. J. Int.*, **171**, 739–754.
- Satoh, T., 2002. Empirical frequency-dependent radiation pattern of the 1998 Miyagiken-Nanbu earthquake in Japan, *Bull. seism. Soc. Am.*, **92**, 1032–1039.
- Somerville, P. et al., 1999. Characterizing crustal earthquake slip models for the prediction of strong ground motion, *Seism. Res. Lett.*, **70**, 59–80.
- Thouvenot, F., Fréchet, J., Jenatton, L. & Gamond, J.F., 2003. The Belledonne border fault: identification of an active seismic strike-slip fault in the Western Alps, *Geophys. J. Int.*, **155**, 174–192.
- Tinti, E., Fukuyama, E., Piatanesi, A. & Cocco, M., 2005. A kinematic source-time function compatible with earthquake dynamics, *Bull. seism. Soc. Am.*, **95**, 1211–1223.
- Tsuno, S., Cornou, C. & Bard, P.Y., 2008. Superficial S-wave velocity and damping factor model determined by the MASW measurement in the Grenoble sedimentary basin, in *The 14th World Conference on Earthquake Engineering*, Beijing, China.
- Tsuno, S., Chaljub, E. & Bard, P.Y., 2009. Grenoble simulation benchmark: Comparison of results and learnings, in *Third International Symposium on the Effects of Surface Geology on Seismic Motion*, Vol. 2, eds Bard, P.Y., Chaljub, E., Cornou, C., Cotton, F. & Guéguen, P., LCPC, 2009. Paper number SB2.
- Vallon, M., 1999. Estimation de l'épaisseur d'alluvions et sédiments quaternaires dans la région grenobloise par inversion des anomalies gravimétriques (estimation of the alluvial and quaternary sediments thicknesses in the Grenoble region from inversion of gravimetric anomalies). Technical report, LGGE, Université Joseph Fourier, IPSN/CNRS, in French.
- Zhao, L., Chen, P. & Jordan, T.H., 2006. Strain Green tensor, reciprocity, and their applications to seismic source and structure studies, *Bull. seism. Soc. Am.*, **96**, 1753–1763.

## APPENDIX A: STATIC SLIP GENERATION

The static slip models are obtained by inverse Fourier transform from eq. (1). They result from the superposition of a deterministic

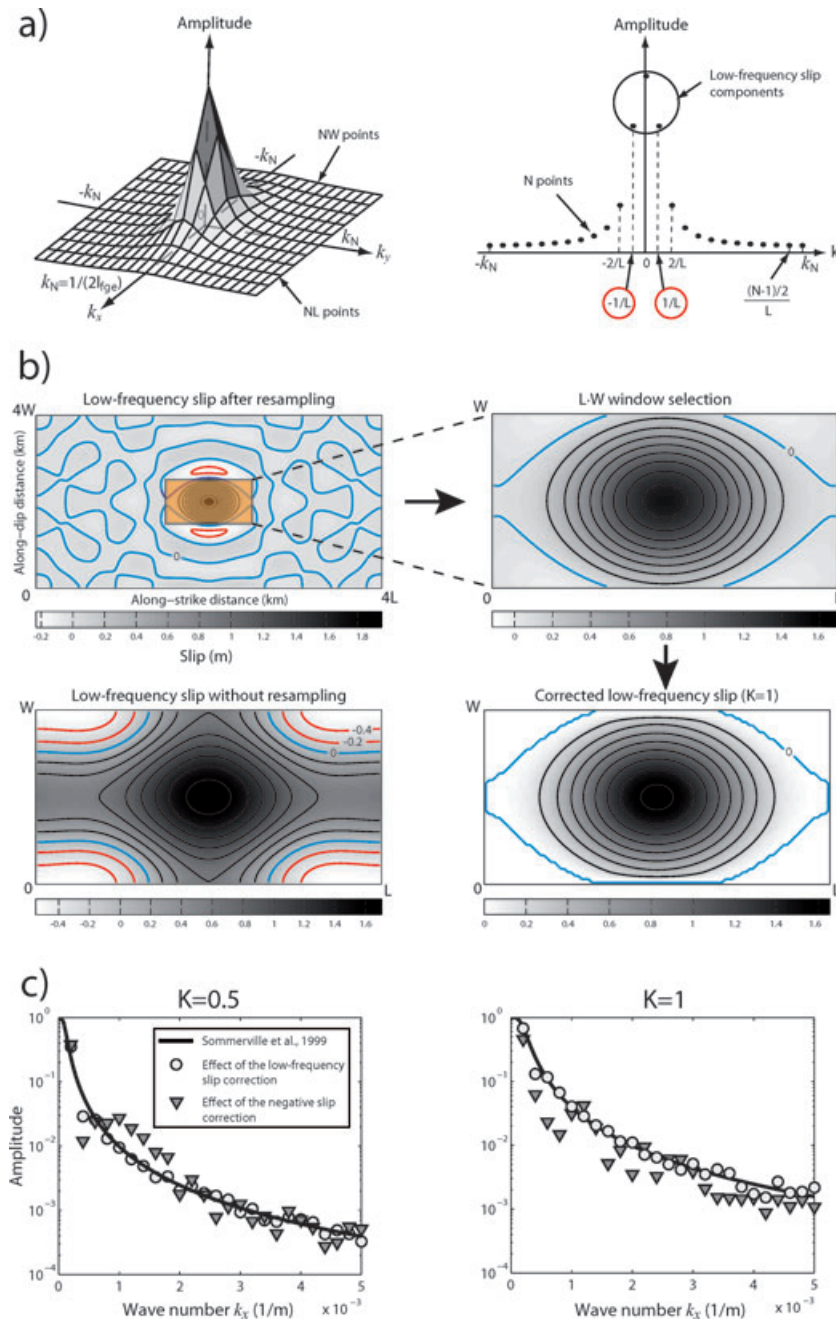


**Figure 14.** (a) Slip amplitude spectrum in 2-D (left-hand panel) and 1-D (right-hand panel). The deterministic slip ( $k \leq 1/L$ ) is defined by only 3 points. (b) Deterministic slip correction procedure. The mean slip is 0.4 m and the  $K$  value equals 1. The space between the slip contourlines is 0.2 m. (c) Effect of the slip correction procedure on the amplitude slip spectrum. The curves correspond to the 1-D along-strike Fourier transforms. The larger the  $K$  value is, the larger the reduction induced by removing the negative slip is.

part ( $k \leq k_c$ ) and a stochastic part ( $k > k_c$ ). From numerical considerations the deterministic slip is defined in the Fourier domain by a limited number of points (only three points in 1-D, Fig. 14a). This results in spurious artefacts in the space domain, in particular strongly negative slip zones. A simple process is thus introduced to enhance the low wavenumber asperity features (Fig. 14b): (1) the low wavenumber slip amplitude spectrum is resampled using  $n$  times the original sampling rate. The resulting spatial slip covers a fictitious fault plane of size ( $nL, nW$ ). In practice, we used  $n = 4$ ; (2) the centre window of size ( $L, W$ ) is selected; (3) the remaining negative slip areas and the fault edges are assigned zero slip and

(4) a constant scaling factor is applied to conserve the mean slip. This procedure brings about only minor modifications on the slip amplitude spectrum (Fig. 14c).

The deterministic slip is next added the high wavenumber slip contributions. A classical problem of this superposition is the emergence of negative slip areas in the final slip distributions. In order to remove the unphysical negative slip values, the slip fluctuation amplitudes are just reduced at any point with negative slip to reach a zero slip. The slip is next tapered on the edges and normalized again to get the right mean slip. The effect of the negative slip removing is to decrease the slip spectrum amplitude at high frequency, and

consequently the source energy. However, this reduction remains weak for  $K \leq 1$  because most of the slip is positive (Fig. 14c). Besides our tests show that the apparent source time function spectral decay is preserved and that the high-frequency energy decrease is also weak for  $K \leq 1$  (cf. Section ‘Summation Algorithm’, Fig. 4e). For simulating with higher  $K$  values, negative slip values can be kept but the  $k^{-2}$  source model has to be considered as a purely mathematical tool providing the expected source spectrum characteristics.

## APPENDIX B: CALCULATION OF THE THEORETICAL ASTF HIGH-FREQUENCY SPECTRAL LEVEL

From eq. (11), the ASTF amplitude spectrum is such that:

$$|R(f)| = |U(f)|/|u(f)|, \quad (\text{B1})$$

where  $U(f)$  and  $u(f)$  denotes the simulated event and the EGF displacement spectra, respectively. Beyond the EGF corner frequency  $f_c$ , both events have a  $\omega^{-2}$  spectral decay. Hence the theoretical ASTF amplitude spectrum is a plateau, the level of which is:

$$|R(f \geq f_c)|_{\text{theo}} = |U(f_c)|_{\text{theo}}/|u(f_c)|_{\text{theo}}. \quad (\text{B2})$$

The theoretical displacement spectrum amplitude of the target event at frequency  $f_c$  is

$$|U(f_c)|_{\text{theo}} = \frac{A_0}{4\pi^2 f_c^2}. \quad (\text{B3})$$

The  $A_0$  value is given by eq. (5) and the corner frequency of the small event, that is assumed to follow a  $k^{-2}$  model, is such that:  $f_c = \frac{vK_S}{l}$ , with  $K_S \approx 0.74$  (eq. 8).

Besides, the propagation effects and radiation patterns and supposed to be the same for both EGF and simulated event. It leads to:

$$|u(f_c)|_{\text{theo}} = C_s m_0, \quad (\text{B4})$$

After eqs (B2), (B3) and (B4), and by assuming that both events have the same rupture velocity, we obtain

$$|R(f \geq f_c)|_{\text{theo}} = \text{RMS} [C_d(\Theta)^2 X(C_d(\Theta)/2)] \left(\frac{M_0}{m_0}\right) \left(\frac{l}{L}\right)^2 \left(\frac{K}{K_S}\right)^2. \quad (\text{B5})$$

For a ratio  $v/c = 0.8$  and for a Gaussian slip velocity function with a standard deviation  $\sigma = \tau/10$   $\text{RMS}[C_d(\Theta)^2 X(C_d(\Theta)/2)] \approx 1.9$ . Thus, eq. (B5) gives

$$|R(f_c)|_{\text{theo}} = \beta N K^2, \quad (\text{B6})$$

with  $\beta \approx 3.5$ .

## APPENDIX C: CALCULATION OF THE EGF NUMBER TO SUM FOR THE HIGH-FREQUENCY ASTF LEVEL CORRECTION

In order to obtain the expected level  $|R(f \geq f_c)|_{\text{theo}}$ , the average number of EGFs to sum along the rise time dislocation is adapted. This choice comes to assume a new EGF dislocation. Let  $d/\gamma$  be the modified EGF dislocation. At low frequency, the EGF summing up is coherent. Hence the ASTF amplitude becomes  $\gamma N^3$ . To conserve

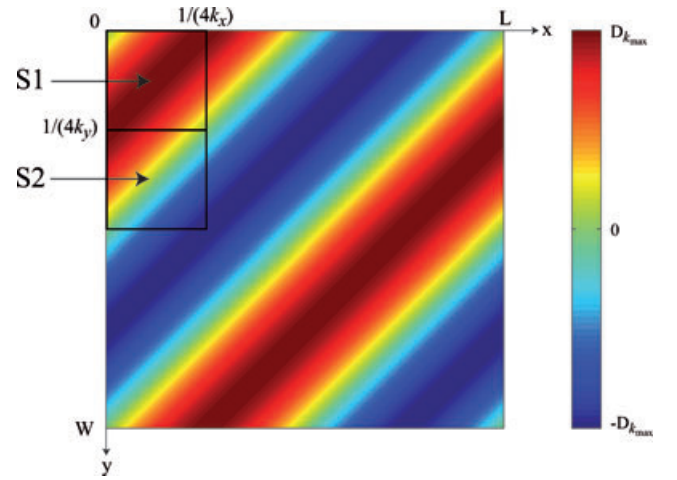


**Figure 15.** Representation of the slip distribution  $D_k(x, y)$  for a given wavenumber  $k$ . The integrals  $I_1$  and  $I_2$  (eqs 26 and 27) represents the integrals of  $|D_k(x, y)|$  over the surfaces  $S_1$  and  $S_2$ , respectively.

the seismic moment, the whole spectrum is divided by  $\gamma$ . Besides, beyond  $f_c$ , the summation is incoherent. Therefore, the ASTF level becomes the square root of the EGF quadratic sum, each EGF being represented by a Dirac function with amplitude 1 or  $-1$ . This leads to

$$|R(f \geq f_c)|_{\text{obs}} = \frac{1}{\gamma} \sqrt{\gamma(N_{\text{STO}} + N_{\text{DET}})}, \quad (\text{C1})$$

where  $N_{\text{DET}} = N^3$  and  $N_{\text{STO}}$  is the total number of summed EGF resulting from the stochastic slip heterogeneities. The deterministic slip contribution to the ASTF is low-pass filtered to keep only the stochastic slip contributions beyond  $f_c$ . Thus, eq. (C1) gives

$$|R(f \geq f_c)|_{\text{obs}} = \left(\frac{N_{\text{STO}}}{\gamma}\right)^{1/2}. \quad (\text{C2})$$

### $N_{\text{STO}}$ calculation

In order to estimate  $N_{\text{STO}}$ , the surface slip density for a given wavenumber  $k > 1/\sqrt{L^2 + W^2}$  is calculated. It is defined as

$$\rho_{s_k} = \frac{1}{LW} \int_0^L \int_0^W |D_k(x, y)| dx dy, \quad (\text{C3})$$

where  $D_k(x, y)$  represents the slip distribution for the wavenumber  $k$ . Using the integrals  $I_1$  and  $I_2$  of  $|D_k(x, y)|$  over the surfaces  $S_1$  and  $S_2$ , respectively (Fig. 15), we obtain

$$\begin{aligned} \rho_{s_k} &= \frac{1}{LW} \cdot 2(I_1 + I_2) \cdot 2Lk_x \cdot 2Wk_y \\ &= 8k_x k_y (I_1 + I_2), \end{aligned} \quad (\text{C4})$$

with

$$\begin{aligned} I_1 &= 2D_k(k_x, k_y) \int_0^{\frac{1}{4k_x}} \int_0^{\frac{1}{4k_y}} |\sin[2\pi(k_x x + k_y y)]| dx dy \\ &= \frac{D_k(k_x, k_y)}{\pi^2 k_x k_y} \end{aligned} \quad (\text{C5})$$

and

$$\begin{aligned} I_2 &= 2D_k(k_x, k_y) \int_0^{\frac{1}{4k_y}} \int_0^{\frac{1}{4k_x} - \frac{k_y}{k_x}} |\cos[2\pi(k_x x + k_y y)]| dx dy \\ &= \frac{(\pi - 2) D_k(k_x, k_y)}{2 \pi^2 k_x k_y}. \end{aligned} \quad (\text{C6})$$

It leads to

$$\rho_{s_k} = \frac{4D_k(k_x, k_y)}{\pi}. \quad (C7)$$

The overall surfacic slip density  $\rho_s$  is obtain by summing all the high wavenumber contributions

$$\rho_s = 2 \int_{k_{x\min}}^{k_{x\max}} \int_{k_{y\min}}^{k_{y\max}} \rho_{s_k} dk_x dk_y. \quad (C8)$$

From eq. (1) we come to

$$\rho_s \approx \frac{8}{\pi} DK^2 \int_{k_{x\min}}^{k_{x\max}} \int_{k_{y\min}}^{k_{y\max}} \frac{1}{k_x^2 + k_y^2} dk_x dk_y. \quad (C9)$$

In the following a square fault plane is assumed ( $L = W$ ). Hence from numerical considerations (see Appendix A, Fig. 14a):  $k_{x\min} = k_{y\min} = \frac{2}{l(N-1)}$  and  $k_{x\max} = k_{y\max} = k_N = \frac{1}{2l}$ . Next cartesian coordinates are replaced with polar coordinates ( $r, \Theta$ ) in eq. (C9). It leads to the following approximation:

$$\begin{aligned} \rho_s &\approx \frac{8}{\pi} \bar{D} K^2 \int_0^{\pi/2} \int_{\frac{2}{l(N-1)}}^{\frac{1}{2l}} \frac{1}{r^2 \cos^2 \Theta + r^2 \sin^2 \Theta} r dr d\Theta \\ &\approx 4\bar{D} K^2 \ln\left(\frac{N-1}{4}\right). \end{aligned} \quad (C10)$$

Besides  $N_{\text{STO}}$  is related to  $\rho_s$  according to

$$N_{\text{STO}} = \frac{\rho_s L^2}{d l^2}. \quad (C11)$$

Then, inserting (C10) into (C11) we get

$$N_{\text{STO}} \approx \alpha(N)^2 N^3 K^2, \quad (C12)$$

with  $\alpha(N) = 2\sqrt{\ln\left(\frac{N-1}{4}\right)}$ .

► *Calculation of the adapted EGF dislocation  $d/\gamma$*

After eqs (C2) and (C12), the observed ATSF spectral level is:

$$|R(f \geq f_c)|_{\text{obs}} = \frac{\alpha(N)}{\gamma^{1/2}} N^{3/2} K. \quad (C13)$$

Finally, after eq. (B6), the condition:  $|R(f \geq f_c)|_{\text{obs}} = |R(f_c)|_{\text{theo}}$  leads to

$$\frac{\alpha(N)}{\gamma^{1/2}} N^{3/2} K = \beta N K^2. \quad (C14)$$

Consequently, the new EGF dislocation to be considered is  $d/\gamma$  with

$$\gamma = \left(\frac{\alpha(N)}{\beta}\right)^2 \frac{N}{K^2}, \quad (C15)$$

where  $\alpha(N) = 2\sqrt{\ln\left(\frac{N-1}{4}\right)}$  and  $\beta \approx 3.5$ .